Summary of Propagation Cases of the Third AIAA Sonic Boom Prediction Workshop

Sriram K. Rallabhandi* and Alexandra Loubeau†
NASA Langley Research Center, Hampton, VA, 23681

A summary is provided for the propagation portion of the Third AIAA Sonic Boom Prediction Workshop held January 5, 2020 in conjunction with the AIAA SciTech 2020 conference. Near-field pressure waveforms for two cases were supplied at multiple azimuthal angles. Ground signatures across the breadth of the sonic boom primary carpet and their corresponding loudness metrics were requested. Each case had some required, as well as some optional, runs. The required cases included atmospheric profiles with measured data including winds. Optional cases included a level-acceleration sonic boom focusing case as well as prediction under standard atmospheric conditions. Participants provided ground signatures along with several loudness metrics using their best sonic boom prediction practices. All the participants' submissions are compared and discussed for each case. Noise or loudness measures are calculated and detailed comparisons and statistical analyses are performed and presented. Compared to previous workshops, the selected cases in the current workshop have much lower boom loudness levels. As was observed in the past workshops, the variation in the loudness measures and spread between participants' submissions increased as the computation proceeded from under-track locations towards the lateral cut-off. Lessons learned during this workshop are discussed and recommendations are made for potential improvements and possible subsequent workshops as we collectively attempt to refine our analysis methods.

I. Nomenclature

ASEL	=	A-weighted Sound Exposure Level
BSEL	=	B-weighted Sound Exposure Level
CSEL	=	C-weighted Sound Exposure Level
DSEL	=	D-weighted Sound Exposure Level
ESEL	=	E-weighted Sound Exposure Level
f_{ac}	=	Characteristic acoustic frequency of the incoming waveform
ISBAP	=	Indoor Sonic Boom Annoyance Predictor
L	=	Aircraft Length
LNTE	=	Lossy Nonlinear Tricomi Equation
M	=	Mach number
$\frac{dM}{dt}$	=	Rate of change of Mach number
$\frac{d^2M}{dt^2}$	=	Rate of change of $\frac{dM}{dt}$
PL	=	Perceived Level
rh	=	Relative humidity (%)
R	=	Radius of near-field cylinder
R_{cau}	=	Radius of curvature of the caustic surface
R_{ray}	=	Radius of curvature of the caustic ray
R_{tot}	=	Relative radius of curvature
SPL	=	Sound Pressure Level
T	=	Atmospheric temperature (°C)
t	=	Time variable
$\overline{Z}$	=	Non-dimensional parameter of the focal region computational domain

*Aerospace Engineer, Aeronautics Systems Analysis Branch, Mail Stop 442, and AIAA Associate Fellow
†Research Aerospace Engineer, Structural Acoustics Branch, Research Directorate, MS 463

δ = Diffraction boundary layer thickness
ϕ,PHI = Azimuthal angle of propagation

II. Introduction and Motivation

The Third American Institute of Aeronautics and Astronautics (AIAA) Sonic Boom Prediction Workshop (SBPW3) was held on January 4-5, 2020 in Orlando, Florida. This workshop was a sequel to the first (SBPW1) [1] and second (SBPW2) [2, 3] workshops held in the past several years. There were approximately 75 attendees and 12 participants in the propagation part of the workshop. The motivations for this workshop were to a) impartially compare propagated signatures from multiple teams/codes under standard and non-standard atmospheric conditions, b) understand the state of current boom prediction methods across the international sonic boom community, and c) explore the effect of the atmosphere on the evolution of shaped sonic booms. The primary objectives of this workshop were to a) aid in the development of a supersonic aircraft noise certification standard, b) verify analysis techniques within multiple codes across international teams, c) understand modeling gaps, and d) improve awareness of sonic boom physics at realistic atmospheric conditions, particularly at lateral cut-offs.

Since the goal of the sonic boom community is to understand how sonic booms are perceived by humans and minimize their impact, a detailed comparison of the participant submissions is included in this paper. This includes sonic boom ground signatures across the primary boom carpet as well as loudness metric analysis. Statistical analysis of the loudness or noise metrics corresponding to the submissions is included not only as a means to identify outlier submissions but also to gain an understanding of the spread in the underlying data. A website * was used to organize the workshop and disseminate results. This includes all the participant presentations, computational meshes for the Computational Fluid Dynamics (CFD) portion of the workshop, and all the submitted results to encourage continued research. Multiple workshop participants also published details of their analyses in conference papers organized into an invited special session at the AIAA SciTech 2021 conference. The data and statistical analyses included in this summary are intended to contribute toward the discussion pertaining to overland supersonic flight by building a consensus in terms of analysis methods and modeling gaps and providing information to aid in developing a certification standard.

A brief introduction to the sonic boom prediction process is provided in Fig. 1, where the computational domain is separated into near-field, mid-field, and far-field. The near-field is a cylindrical zone a few (typically 3 to 5) body-lengths around the aircraft. This zone has many nonlinear and three-dimensional interactions of shock disturbances from the aircraft and is typically analyzed using CFD. The first day of SBPW3 was dedicated to this portion of the sonic boom prediction process, and discussion of those cases and results is summarized in other papers [4, 5]. Once the near-field waveform is determined using CFD, the waveform has to pass through long stretches of the atmosphere (mid-field and far-field domains) while being modified due to the physical mechanisms as well as pushed around due to prevailing winds. The far-field typically also involves a planetary boundary layer that has the potential to distort the underlying waveform by introducing random ripples as a result of interactions with prevailing atmospheric turbulent fluctuations. For the SBPW3 workshop and results provided in this paper, the near-field CFD pressure waveforms are propagated to the ground ignoring turbulent interactions in the planetary boundary layer and assuming the CFD cylinder is sufficiently far away from the aircraft such that planar wave propagation approximations hold true. However, participants were free to implement other techniques [6–9] to account for any three-dimensional effects in the provided near-field pressure waveforms.

A. Cases for propagation

Before the propagation cases were down-selected, discussions were held to finalize the nature and number of cases to be included in the workshop. A sonic boom prediction workshop committee consisting of sonic boom experts from industry, academia, and research organizations from across the world were asked for their input in crafting the propagation cases and the desired outputs. Building upon the lessons learned from earlier workshops, it was determined that past submissions had larger spread at the edges of the primary carpet. In addition, previous workshops only included simulations of cruise booms. To overcome these shortcomings, the third sonic boom prediction workshop not only included two required cases to predict cruise booms corresponding to much quieter concepts, but it also included an optional focus boom simulation. The primary areas of comparison in this workshop were juxtaposing participants' submissions of ground signatures and other sonic boom metrics a) at under-track and off-track azimuthal

*https://lbpw.larc.nasa.gov

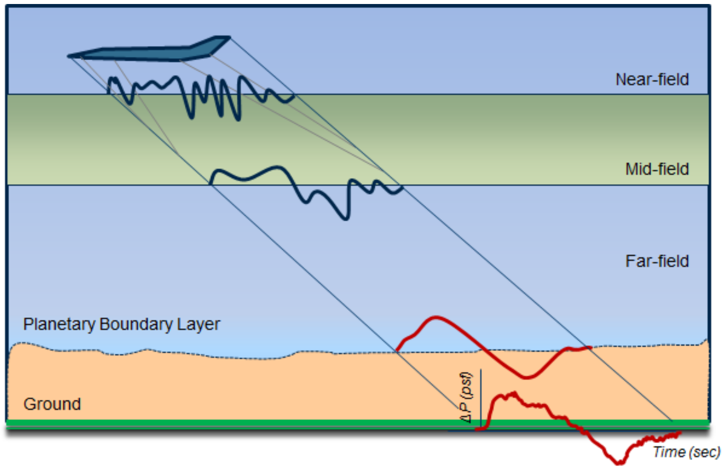

Fig. 1 Sonic boom prediction process [10].

angles, including near lateral cut-offs, under non-standard and standard atmospheric profiles and b) corresponding to the level-acceleration sonic boom focusing. The two vehicle concepts used in the workshop are briefly described below.

1. Case 1: C25P

The first concept being investigated for sonic boom analysis is shown in Fig. 2(a) and the off-body pressure waveform (often referred to as the *near-field pressure waveform*) corresponding to that concept is shown in Fig. 2(b). For the sake of de-cluttering, data corresponding to only some selected azimuthal angles are shown; however, CFD near-field data were provided at azimuthal angles ranging from $-90°$ to $90°$ in $10°$ increments. The flight is assumed to be cruising at M=1.6 and an altitude of 15,760 meters. The CFD pressure was supplied on a cylinder with a radius of 100.584 meters (R/L = 3.0) around the aircraft concept and the ground altitude was specified to be 264.09 meters based on the lowest altitide in the chosen atmospheric profile. For all the simulations, a ground reflection factor of 1.9 is used.

(a) **NASA Concept C25P.**

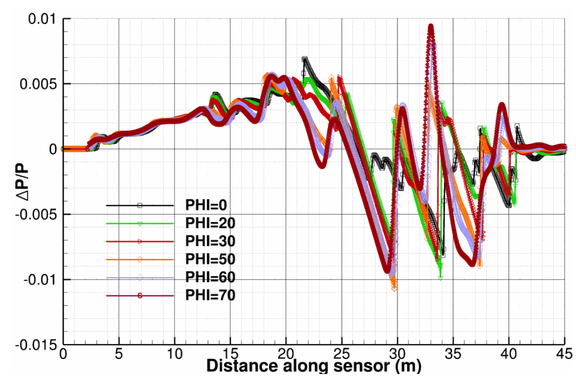

(b) **C25P near-field pressures.**

Fig. 2 Case 1: C25P.

2. Case 2: C609

The second case used in the workshop is a variant of the X-59 Low Boom Flight Demonstrator (LBFD) aircraft referred internally as C609. The Lockheed Martin Corporation (LM) has been awarded a contract to manufacture the X-59 to demonstrate unique boom shaping technologies and address system integration challenges associated with limiting maximum sonic boom Perceived Level (PL) of loudness to less than 75 dB across the entire carpet while flying at a Mach number of 1.4 and an altitude of 16,459.2 meters. Initial flights of the X-59 are expected to begin in the

2021-2022 time frame, with validation flights and community tests expected at multiple locations following the flight envelope expansion. Figure 3(a) depicts a rendering of the concept used in this study, and Fig. 3(b) shows the near-field pressure waveforms at selected azimuthal angles. Detailed CFD pressures were provided at every 2° degrees spanning from −90° to 90°. The CFD pressure was supplied on a cylinder with a radius of 82.296 meters (R/L = 3.0) around the aircraft concept and the ground altitude was specified to be 110.01 meters, which is again based on the lowest altitide in the chosen atmospheric profile.

(a) **Low Boom Flight Demonstrator Variant C609.**

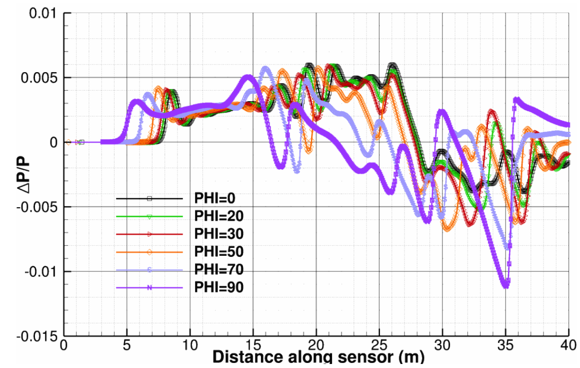

(b) **C609 near-field pressures.**

Fig. 3 Case 2: C609.

The propagation simulations were required to be run using prescribed non-standard atmospheric conditions. The idea was to rigorously test the ray path integration and implementation of the underlying physical mechanisms under realistic windy conditions.

B. Selection of Atmospheric Conditions

Previous sonic boom workshops have shown that participants' submissions were different when the underlying atmospheres were non-standard with non-zero wind conditions. For the current workshop, atmospheric profiles are drawn from the Climate Forecast System Reanalysis (CFSR) database [11]. This database assimilates data over long durations using multiple models with the intent of creating a global state-of-the-art representation of the underlying atmospheric states by removing fictitious trends in real-time measurements. The spatial resolution of the data used is 0.5° in both latitude and longitude, which translates to roughly 56 km separation between adjacent locations within the database. The temporal resolution of the data is every 6 hours; the vertical resolution consists of 37 isobaric pressure levels. For this study, a subset of the database has been queried over the past 5 years to determine atmospheres that produce a) a physically narrow/medium/wide east-heading carpet, b) a low/medium/high loudness corresponding to an east-heading carpet, and c) an angularly narrow/medium/wide east-heading carpet. For Case 1, an atmospheric profile producing the angularly widest carpet (see Fig. 4(a)) was picked, whereas for Case 2, an atmosphere that generated a physically wide carpet was selected (Fig. 4(b)). Figures 5(a) and 5(b) depict the temperature, relative humidity, and winds for Case 1 and Case 2, respectively, along with the standard atmospheric profiles. Also included are the cruise altitudes for each of the cases depicted as a horizontal line running across the width of the plot.

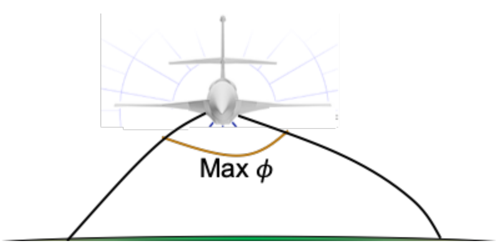

(a) **Criterion for selection for Case 1.**

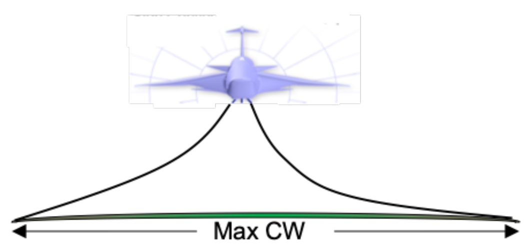

(b) **Criterion for selection for Case 2.**

Fig. 4 Atmospheric profile selection criteria.

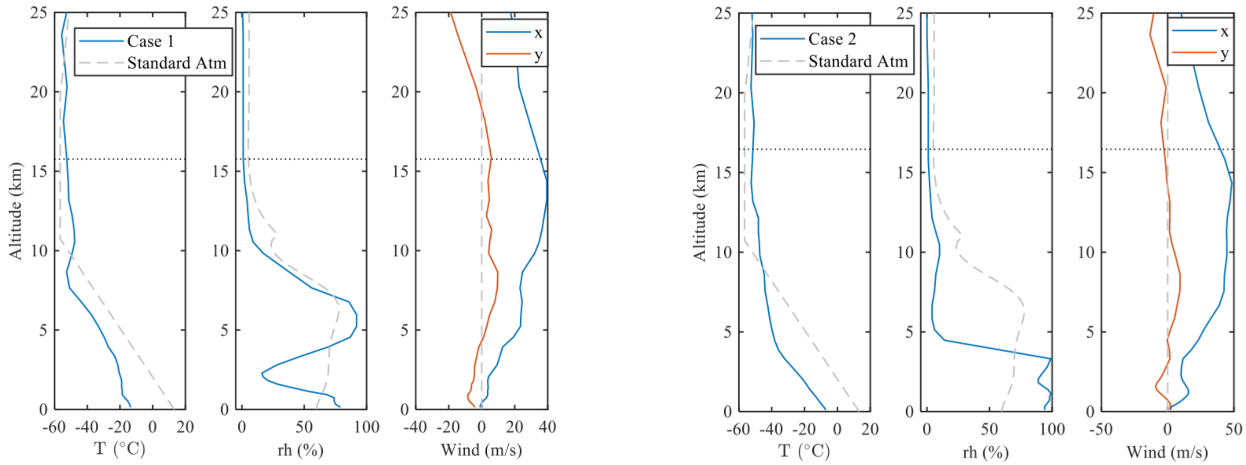

(a) **Case 1 profiles.**

(b) **Case 2 profiles.**

Fig. 5 Chosen atmospheric profiles.

III. Conventions and Evaluation Methods

This section briefly describes the conventions used for the workshop. Azimuthal angle is defined so that from the point of view of the pilot, positive values are to his/her right and negative values are to his/her left. For the wind convention, the positive X-wind is tailwind since the aircraft is flying east for all the simulations in the workshop. Positive Y-wind is going north i.e., from a pilot's point of view, positive Y-wind is blowing toward his/her left. Put another way, if aircraft were flying north, positive Y-wind would be tailwind.

Evaluation of submissions is done in multiple ways, including the ground signatures, loudness metrics, and intersection of the sonic boom disturbances with the ground. Evaluation of the ground intersections compares ray paths, comparison of ground signatures reflects the atmospheric propagation mechanisms along the ray paths, and loudness metrics include the cumulative effect of all sonic boom propagation phenomena. Participants were requested to submit Mark VII Perceived Level (PL) of Stevens [12], A-weighted Sound Exposure Level (ASEL), B-weighted Sound Exposure Level (BSEL) and C-weighted Sound Exposure Level (CSEL). Multiple studies [13, 14] have demonstrated correlation between human annoyance to sonic booms with PL and BSEL. Because psycho-acoustic research is still ongoing to determine the best loudness metric for sonic boom impact, additional measures are calculated to investigate the distribution of submission data. The loudness metrics considered have been shown to correlate well with multiple laboratory datasets of human annoyance to sonic booms in both outdoor and indoor environments [14] and include PL, ASEL, BSEL, DSEL, ESEL, and ISBAP (Indoor Sonic Boom Annoyance Predictor [14]).

IV. Participants

Overall, there were 12 participants that submitted the required cases. All submissions included atmospheric loss mechanisms, of which 6 were based on distinct implementations. This is a slight progression from SBPW2, where at least one of the participants used lossless propagation with tangent hyperbolic rise times added to the shock discontinuities to predict the loudness metrics. Table 1 lists the details of each submission.

Table 1 Submission Index

Participant Index	Noise Metrics	Lateral Cut-off Analysis	Optional Runs	Special Notes
P1	✓	✓	✓	Developer/Power User
P2	✓	✗	✗	Developer/Power User
P3	✓	✓	✗	Developer/Power User
P4	✓	✓	✗	Developer/Power User
P5	✓	✓	✗	
P6	✓	✓	✓	Developer/Power User
P7	✓	✗	✓	Developer/Power User
P8	✓	✗	✗	Developer/Power User
P9	✓	✗	✗	
P10	✓	✗	✗	Power User
P11	✓	✗	✗	Power User
P12	✓	✗	✗	

V. Results and Discussion for Case 1: C25P Sonic Boom Comparison and Analysis

A. Ground Signatures and Loudness Metrics

Figure 6 shows the comparison of the ground signatures at some selected azimuthal angles. All the participants' submissions are overlaid on each other. It is observed that the magnitude of the ground pressure signatures decreases as the boom moves away from the flight track

Each of the submissions is interpolated to a common time grid at each azimuthal angle to compute the mean and point-wise standard deviation estimates. Ground signatures that lie outside one standard deviation from the mean are identified as outliers for this study; however, it is possible that the identified outlier may be capturing physics not being captured by the other submissions. Figure 7 depicts the ground signatures and one standard deviation plots along the flight track as the number of submissions is progressively updated. Initially, mean and standard deviation are computed for the entire ensemble. Submissions that lie significantly outside one standard deviation from the mean are removed to generate the mean and standard deviation of the remaining submissions as depicted in Fig. 7(c). Participant p11's submission was outside the one standard deviation limit and hence is termed as an outlier. Finally, the mean and standard deviation of submissions corresponding to a single code, but likely different versions, are depicted in Fig. 7(d). Because of the continual updates to the underlying algorithm and implementation of the numerical schemes within any particular implementation, the best we can aspire to achieve for the entire ensemble is to reach the spread between submissions using a single code. This simply shows that the understanding of the sonic boom propagation physics and modeling is still evolving as the sonic boom community attempts to understand and model previously unaccounted for phenomena or fine tune their numerical implementations with higher-order effects that were previously either not modeled or not important.

The same process is repeated for an arbitrarily selected azimuthal angle of 40° and depicted in Fig. 8. Two observations can be made regarding these plots. Firstly, the standard deviations increase at the chosen azimuthal angle of 40° compared to those corresponding to the flight track. Secondly, the spread between users of a single code is almost the same magnitude as that corresponding to the full ensemble.

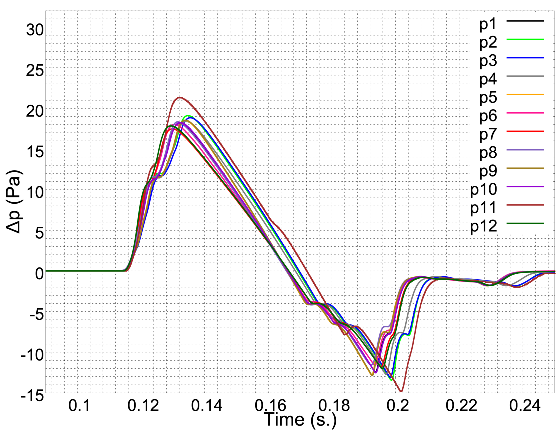

(a) $\phi = 0°$.

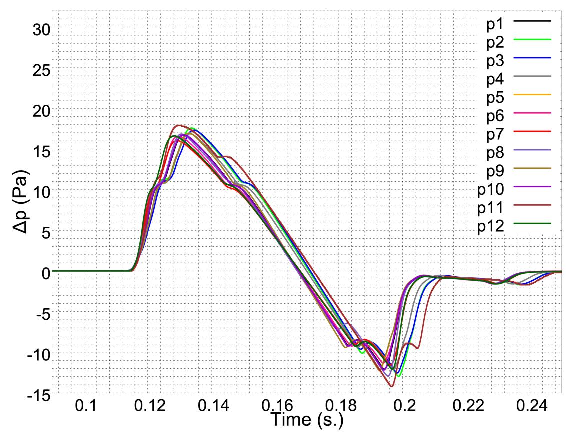

(b) $\phi = 20°$.

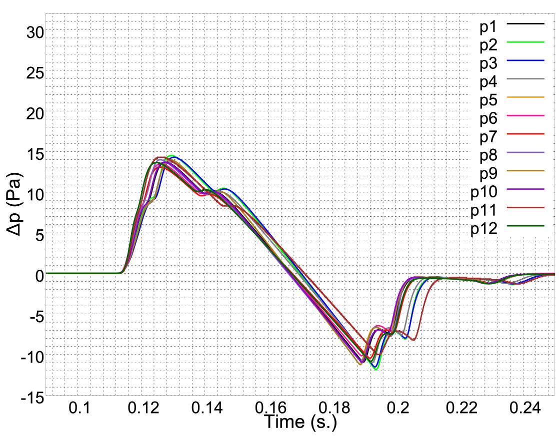

(c) $\phi = 40°$.

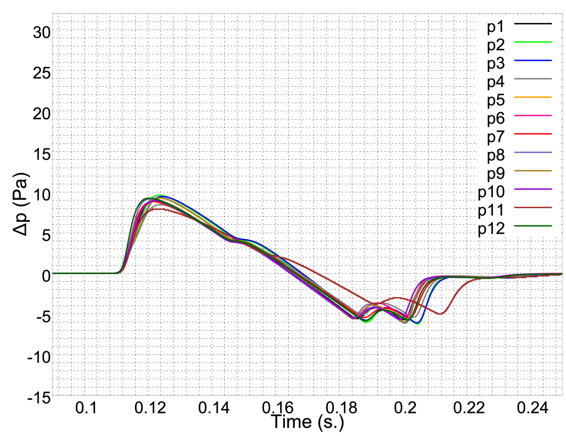

(d) $\phi = 60°$.

Fig. 6 Case 1: Ground signatures.

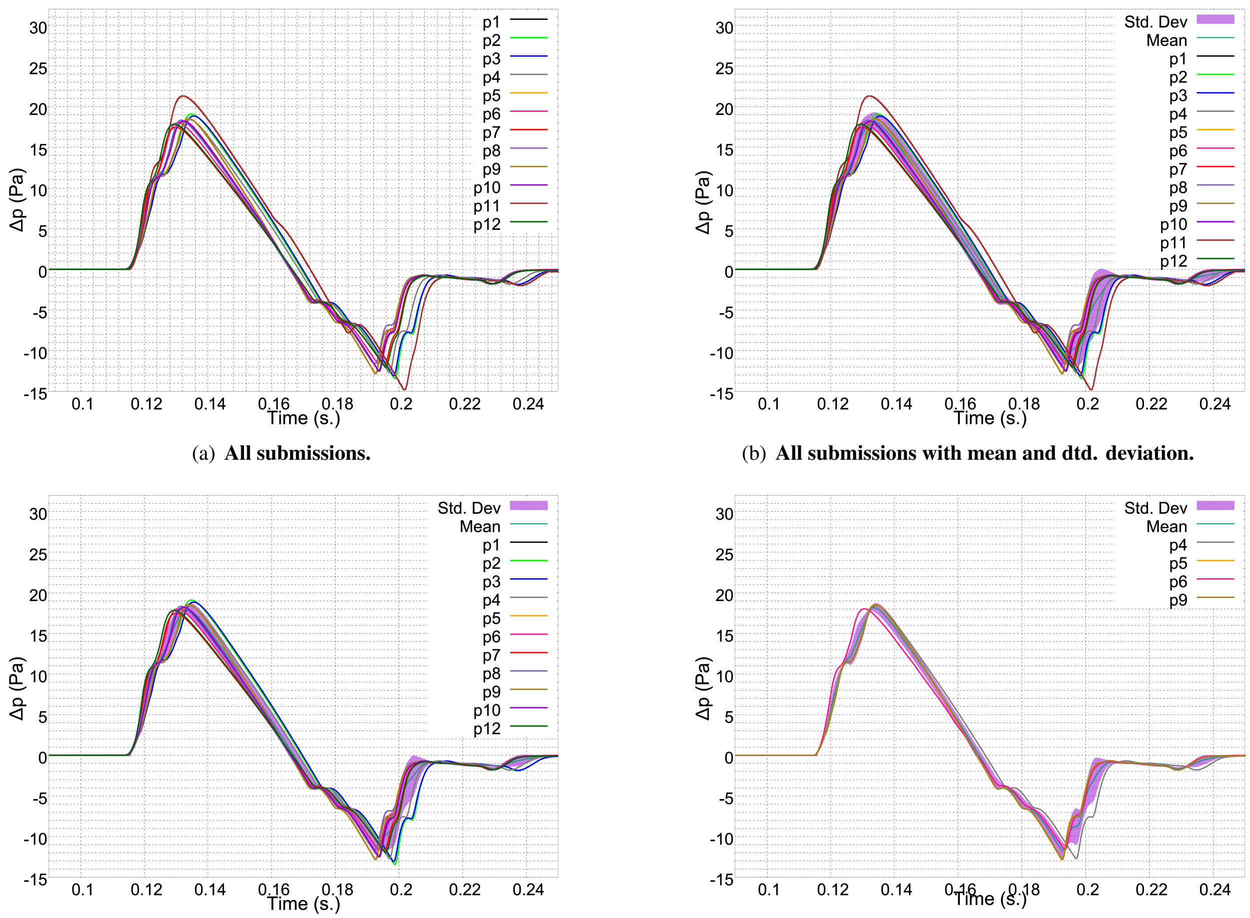

(a) **All submissions.**

(b) **All submissions with mean and dtd. deviation.**

(c) **One standard deviation after removing outliers.**

(d) **One standard deviation using a single code.**

Fig. 7 Case 1: Ground signatures and standard deviation at $\phi = 0°$.

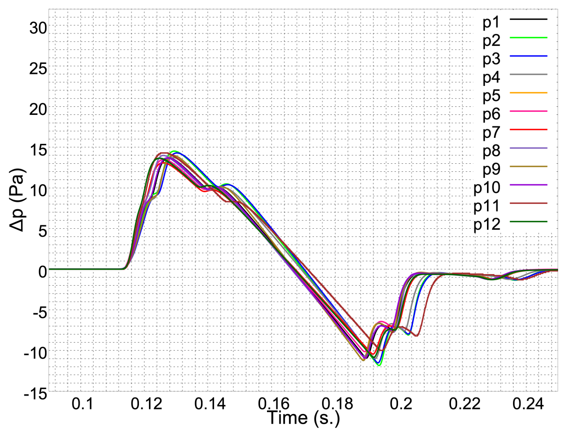

(a) **All submissions.**

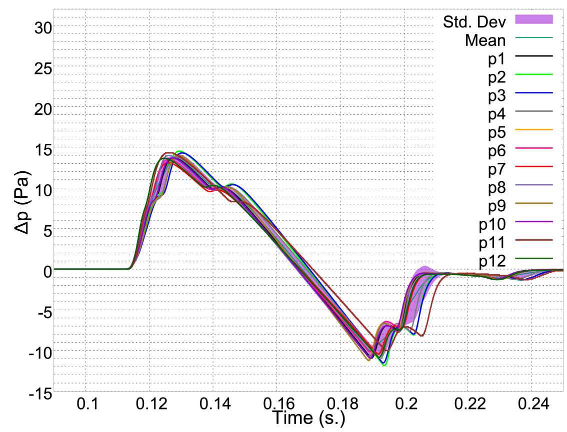

(b) **All submissions with mean and std. deviation.**

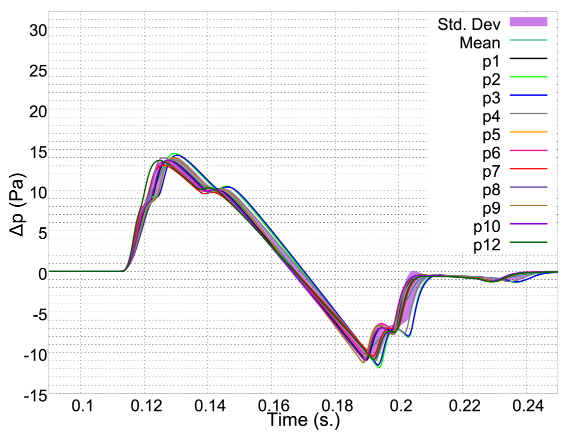

(c) **standard deviation after removing outliers.**

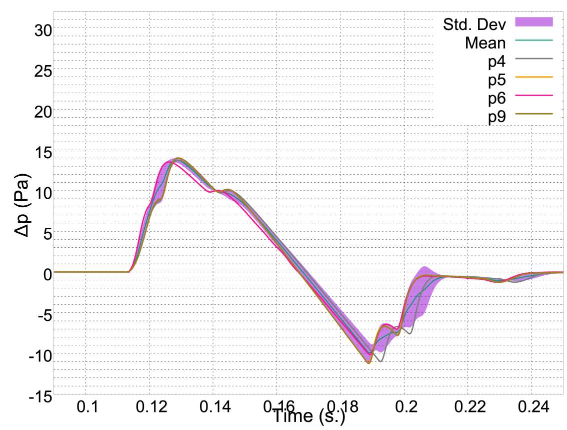

(d) **One standard deviation using a single code.**

Fig. 8 Case 1: Ground signatures and standard deviation at $\phi = 40°$.

The next set of graphs in Fig. 9 depict the loudness carpets of all the participants, which combines the loudness metrics and the lateral ground intersection locations. Although it is unusual to show the loudness metrics on a logarthmic scale because they are already logarthmic values, they are depicted in such a fashion here to be able to plot and compare all the loudness metrics without changing axis ranges. For most of the submissions, lateral distances of [-17, 25] nm correspond to azimuthal angles of [-60°, 60°] respectively; distances beyond those bounds correspond to larger azimuthal angles. The following observations can be made:

1) The PL and BSEL metrics are quite close to each other in terms of magnitude.
2) The spread between participants reduces for BSEL and CSEL compared to PL and ASEL, particularly farther away from flight track.
3) The predicted lateral cut-off azimuthal angles are slightly different for each participant depending upon ray path analysis. At high azimuthal angles, the ray angles are almost horizontal, leading to much larger differences in lateral cut-off ground intersection locations depending on the precision used in the determination of the cut-off angles.
4) The steeper drop in loudness of participant p3 at the lateral edges of the carpet is perhaps a manifestation of lack of data near the edges of the lateral sonic boom carpet.

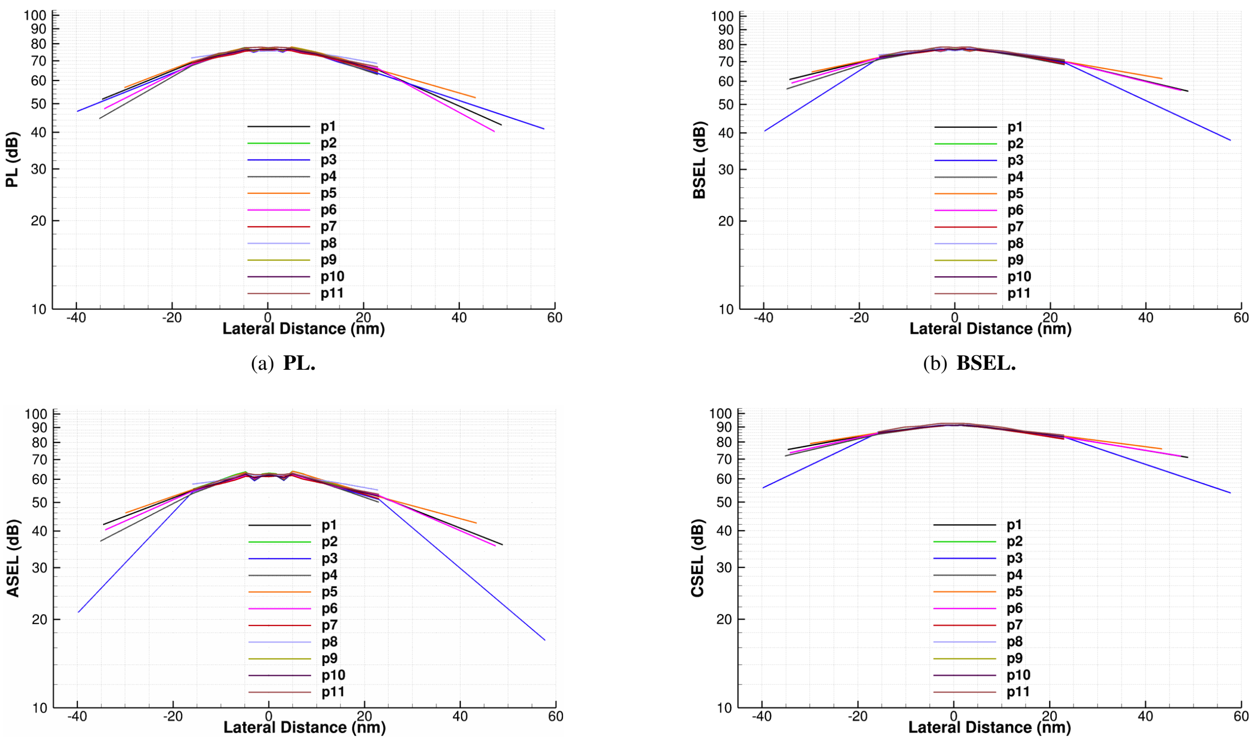

(a) **PL.**

(b) **BSEL.**

(c) **ASEL.**

(d) **CSEL.**

Fig. 9 Case 1: Loudness carpet.

The lateral cut-off angles computed by each participant are listed in Table 2. Each participant, other than participant p12, predicted cut-off angles that are quite close to each other. The small differences are most likely the result of using slightly different angular tolerances when predicting the extent of the lateral carpet; participant p12 did not submit lateral cut-off azimuthal angles. However, based on the lateral carpet edge distances, it is clear that at large angles, small differences in angular tolerances can lead to large discrepancies in ground intersections owing to small grazing angles of the ray paths.

Figure 10 depicts the PL and BSEL of the participant submissions in the inner regions of the carpet, where the discrete points that make the plots are displayed as well. Since the discrete points are all vertically spread along each participant curve, the ground intersection locations can be deduced to be almost identical between participants. The PL spread varies from a minimum of about 2.0 dB along the flight track to a maximum of about 3.0 dB, whereas the BSEL spread varies from a minimum of 1.5 dB to a maximum of around 3.0 dB. Interestingly, the highest spread does

Table 2 Case 1 Lateral Cut-Off Submissions

Participant Index	Lateral Cut-off Angles	Lateral Carpet Edges nm
P1	−78.32°, 68.96°	47.89, -33.63
P2	−78.4°, 68.9°	55.82, -33.98
P3	−78.41°, 69.01°	57.75, -39.82
P4	−78.3°, 69.1°	✗, -35.18
P5	−77.88°, 68.51°	43.46, -29.93
P6	−78.3°, 69.0°	47.38, -34.16
P7	−78.37°, 69.01°	49.55, -35.42
P8	−78.5°, 68.8°	55.67, -35.9
P9	−77.9°, 68.5°	40.33, -29.79
P10	−78.32°, 68.96°	49.38, -35.32
P11	−78.4°, 69.1°	48.88, -34.83

not correspond to the same lateral distance on the ground for the PL and BSEL metrics. Since we determined that participant p11 was an outlier, if we discount that submission, the PL and BSEL spreads across the carpet are in the range [1.5, 3.0] and [0.5, 2.2] dB, respectively.

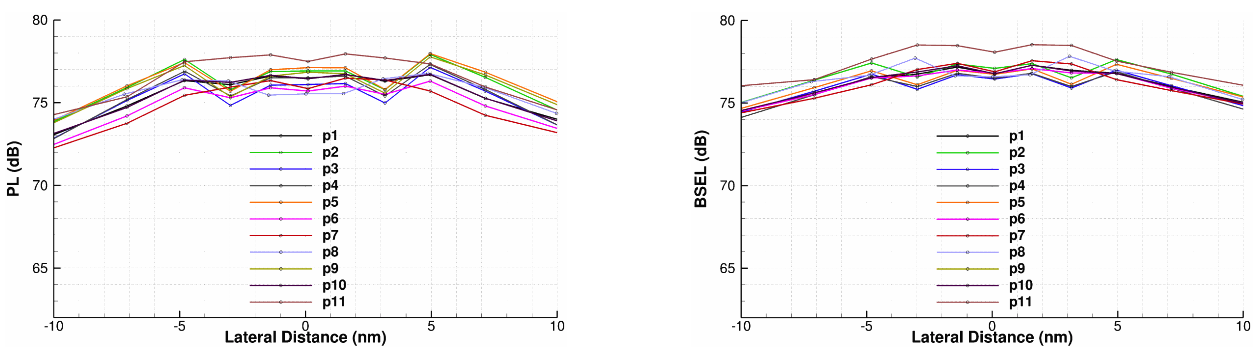

(a) **PL.**

(b) **BSEL.**

Fig. 10 Case 1: Loudness inner carpet.

B. Statistical Analysis

The results can also be analyzed by grouping them by the azimuthal angle of emission from the aircraft near-field. This method allows for observation of the spread of data in boxplots, as shown in Fig. 11. These boxplots show the median, a box covering half the data from 25% to 75%, whiskers that cover ± 2.7 σ (≈99% of the data assuming a normal distribution), and any outliers. In terms of PL, the results for Case 1 in Fig. 11(a) show an outlier (participant p11) at higher metric values for most azimuthal angles. As shown before, the metric values generally decrease with increasing azimuthal angle, while predictions at ± 30° tend to increase slightly. The spread of the data grows as the azimuthal angle increases farther off-track, indicating more differences between codes for the longer ray paths. Because the atmosphere was chosen to result in an angularly wide carpet (Sec. II.B), rays from azimuthal angles of -70° to +60° are predicted to reach the ground; this is much wider than would be expected with a standard atmosphere prediction.

The same results in terms of BSEL are also shown in Fig. 11(b), and all the computed values are much more tightly grouped than for PL. Only one outlier exists at the under-track position. Because this metric is less sensitive to small differences in waveform details, the participant results are all very similar, indicating very good agreement between codes even toward the lateral edge of the wide carpet.

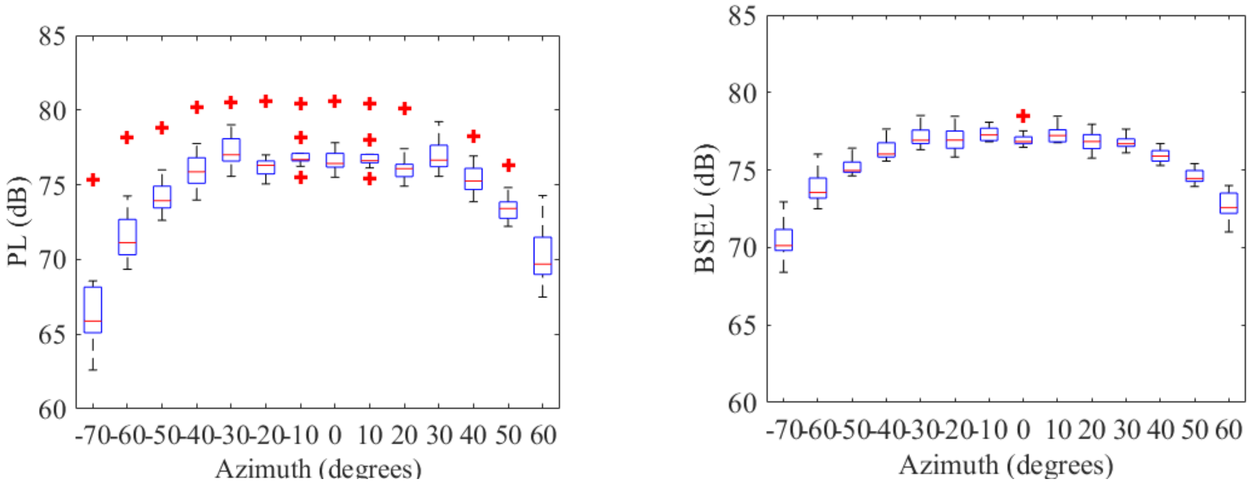

(a) **PL.**

(b) **BSEL.**

Fig. 11 Case 1 PL and BSEL boxplots across the carpet.

The standard deviation of predicted values across participants for each azimuthal angle is shown in Fig. 12 for each of the six metrics considered. All metrics were re-calculated from the submitted waveforms using the same loudness code. One standard deviation represents the distance from the mean that accounts for approximately 34% of the data. The standard deviations with PL are the largest of all the metrics for all angles, ranging from 1.1 dB at +30° to 3.3 dB at -70°. Similar to the boxplot, this shows an increase in standard deviation toward the lateral edges of the carpet, with higher standard deviations at the negative azimuthal side. The metric Indoor Sonic Boom Annoyance Predictor (ISBAP) has the next highest standard deviation, followed by ASEL. The trends are similar to those for PL. The metrics BSEL, DSEL, and ESEL have the lowest standard deviation values and exhibit less variation in standard deviation across the carpet, with values ranging from 0.3 dB to 1.5 dB. These indicate good agreement across participants for all carpet locations considered. Note that the lateral edge of the carpet is not included here, because participants calculated different azimuthal angles for the lateral edge, and several participants did not provide waveform predictions at these locations.

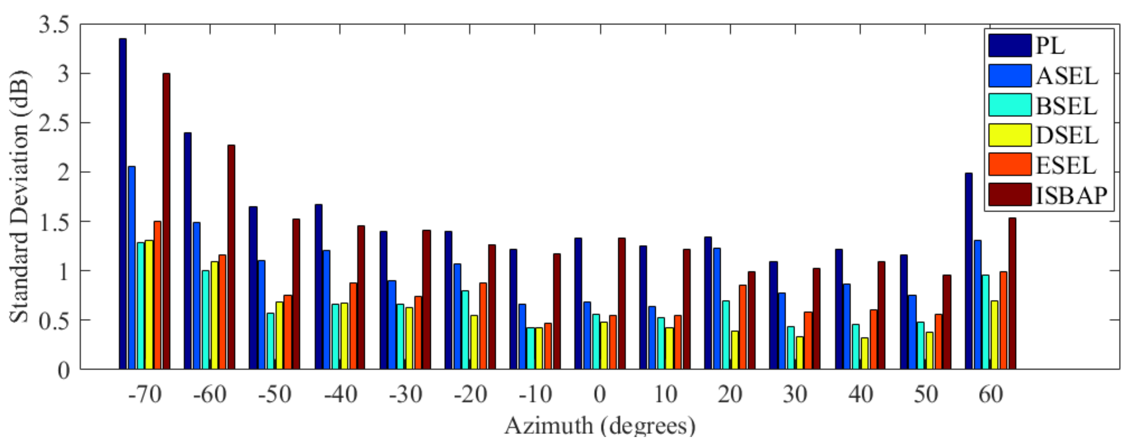

Fig. 12 Case 1 standard deviation of metric values across the carpet.

C. Spectral Analysis

The results from the previous section can be further analyzed by inspecting spectral plots of the waveforms. Each one of the noise metrics is calculated by first converting the pressure-time waveform into sound pressure levels in the frequency domain, and differences between metrics depend on the frequency weighting applied to approximate the frequency sensitivity of human hearing. The spectra in Fig. 13 are collected into one-third-octave frequency bands for the under-track case of $\phi = 0°$. Although most results are very similar, with a peak near 10 Hz and a typical decrease in Sound Pressure Level (SPL) with increasing frequency, the p11 spectrum exhibits an unusual increase in SPL from 1 kHz to 10 kHz, before sharply decreasing. Close inspection of the waveform reveals an oscillation pattern superimposed on the sonic boom. The p8 spectrum also differs from the rest, having a sharper roll-off with frequency above 250 Hz.

Figure 13(b) provides more information by showing the loudness values that are frequency weighted for the PL calculation. It is shown that the increase in SPL in the p11 spectrum results in an increase in loudness in this higher-frequency region, with a peak at 6300 Hz. This is a major factor that contributes to higher PL values for p11, as shown previously in the outliers of Fig. 11. The p8 loudness spectrum does exhibit lower levels above 250 Hz, but the effect is not as pronounced. The result is a lower PL value than the others for this under-track location, but the difference is not large enough to be considered an outlier.

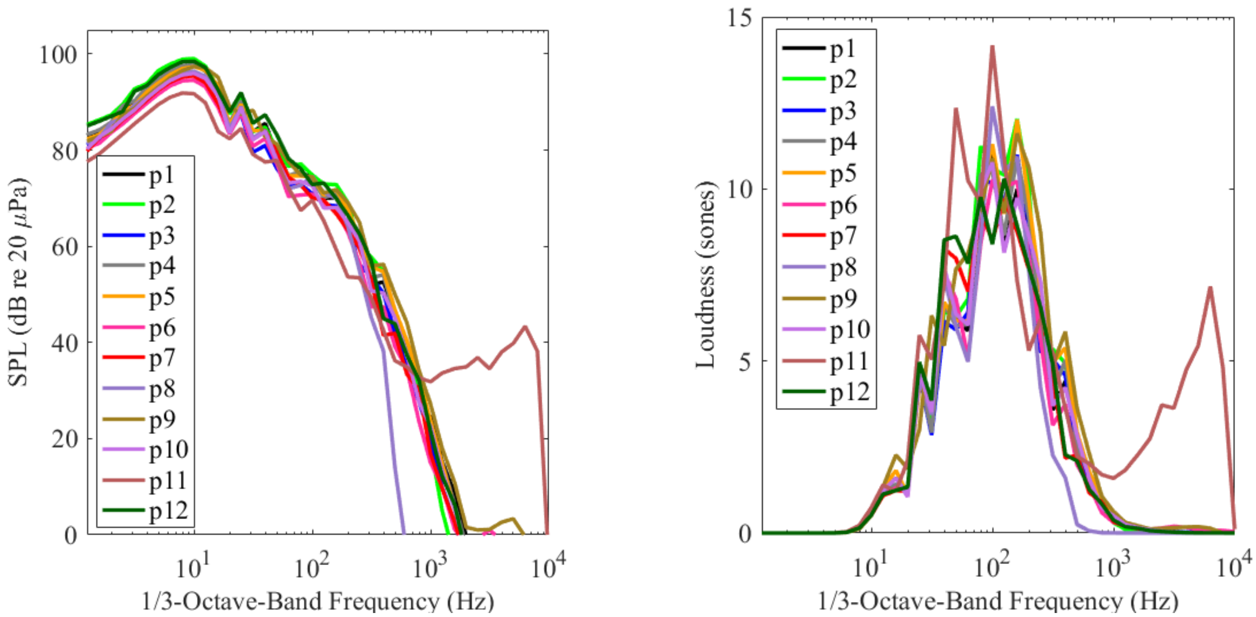

(a) **SPL.** (b) **Loudness.**

Fig. 13 Case 1 Sound Pressure Level (SPL) spectra and loudness spectra for $\phi = 0°$.

D. Optional Level Acceleration Focusing

One of the optional cases included in the workshop was sonic boom focusing prediction corresponding to a level acceleration of $\frac{dM}{dt} = 0.015681$ and $\frac{d^2M}{dt^2} = 0.000359$ at Mach = 1.4121. The near-field starting pressure waveform for this condition is shown in Fig. 14. The starting altitude for propagation is 13,716 meters and the ground is assumed to be at 58 meters.

Three participants (p1, p6, p7) provided results corresponding to this optional case. Results from all three submissions are based on a Burgers solver coupled with the solution of the Lossy Nonlinear Tricomi Equation (LTNE). Participants p1 and p6 based their LNTE analysis on Ref. [15], which was developed as part of the NASA's Superboom Caustic Analysis and Measurement Program (SCAMP) [16]. Participant p7 used their own implementation based on Ref.[17]. During NASA's SCAMP campaign, it was shown that LNTE solver predictions agreed well with experimental data.

The description here discusses the detailed interface between the Burgers solver and LNTE to be able to correctly predict the focus, post-focus, and evanescent waves. Figure 15 shows the underlying process to determine the data hand-off between the two solvers. The caustic line or surface is computed by moving back and forth from the given

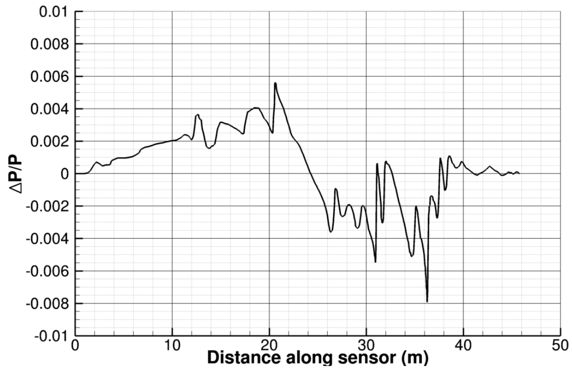

Fig. 14 Case 1: C25P focus near-field pressure.

flight conditions along the flight trajectory and determining the focal points. The locus of the focal points is termed as the caustic line or surface and geometric ray acoustic theory breaks down in regions around this caustic surface. To overcome this shortcoming, the nonlinear Tricomi equation was developed. The discussion below is to set up the computational domain around the caustic surface to predict ground signatures corresponding to a) locations behind the caustic surface (also called evanescent waves), b) locations on the caustic surface (focus booms), and c) locations ahead of the caustic surface (post-focus booms) where reflections off the caustic surface are captured.

The first step in setting up the computational domain for the LNTE is to compute the intersection of the caustic line or surface with the ground (labeled P in the Fig. 15). The caustic tangent ray is then determined as the ray from the vehicle that intersects the ground at the same point as the intersection of the caustic line with the ground. The radius of curvature of the caustic line (R_{cau}) and the radius of curvature of the caustic tangent ray (R_{ray}) are determined. From these values, the total radius of curvature is determined as $\frac{1}{R_{tot}} = \frac{1}{R_{cau}} - \frac{1}{R_{ray}}$. The characteristic frequency (f_{ac}) is computed as the frequency corresponding to the maximum in power spectrum of the incoming waveform. Based on the computational domain of the LNTE solver, the non-dimensional coordinate $\overline{Z}$ may be defined as in Eq. (1). It is the ratio of the normal distance from the caustic line intersection with the ground (Z) to the diffraction boundary layer thickness (δ).

$$\overline{Z} = Z \left[\frac{2 f_{ac}^2}{R_{tot} c_0^2} \right]^{1/3} \tag{1}$$

When $\overline{Z} = 1$, the normal distance would simply be the diffraction boundary layer thickness, which is computed as $\left[\frac{2 f_{ac}^2}{R_{tot} c_0^2} \right]^{-1/3}$. The determination of the delta ray begins with the computation of the point in space δ normal distance away from the caustic line intersection with the ground. This point (say S) is labeled as the interface point between the Burgers and LNTE solvers. The flight conditions when the caustic ray intersects the ground are Mach = 1.4121, Altitude = 45,000 ft, with acceleration of $\frac{dM}{dt} = 0.015681$, and a rate of change of acceleration of $\frac{d^2M}{dt^2} = 0.000359$. Assuming the time along flight trajectory at the caustic tangent ray flight conditions to be 0 (refers to the point labeled "Given (M$\frac{dM}{dt}$, $\frac{d^2M}{dt^2}$)" in Fig. 15), time is advanced incrementally to determine the flight time that makes the corresponding ray, named the delta ray, to pass through S. This point is the origination of the delta ray path and is labeled as "New (M,$\frac{dM}{dt}$, $\frac{d^2M}{dt^2}$)" in Fig. 15.

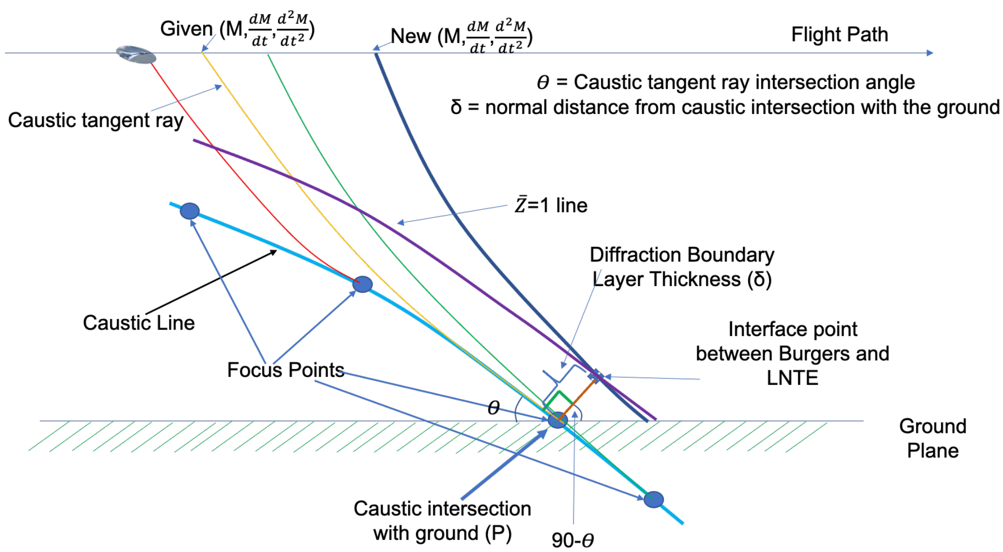

Fig. 15 Focusing geometry during level acceleration.

Burgers propagation is carried out at these updated conditions until an altitude that corresponds to the location that is labeled as the "Interface point between Burgers and LNTE" and the resulting waveform at this location, without the ground reflection factor, is termed as the "incoming waveform." Due to the complex nature of the determination of the delta ray and to keep things consistent between participants, it was decided to use the caustic tangent ray as the interface hand-off between Burgers and LNTE during the workshop. Since the workshop, interactions between participants who submitted the optional focus case has resulted in properly modeling the focus booms through the use of delta ray conditions to interface the Burgers and LNTE domains. However, each of the participants computed different values for the characteristic frequencies and caustic geometries leading to differences in the diffraction boundary layer thickness values and therefore the computation of the delta ray. After the workshop concluded, to simplify comparisons, the diffraction boundary layer thickness (δ) was fixed at 302.4 meters ensuring that the projected time advance in the aircraft trajectory and the flight conditions corresponding to the delta ray condition were consistent between participants. All participants were asked to use this prescribed δ value to determine the delta ray conditions to propagate using their respective Burgers implementations to determine the incoming waveform at the interface location with the LNTE domain. The participants then used their computed value of f_{ac} from their Burgers propagated solutions and the prescribed value of δ to calculate the total radius of curvature (R_{tot}), rather than computing it from the caustic geometry as described above. This ensured that the non-dimensional distances corresponded to the same physical locations in the LNTE computational domain and the results were consistent between submissions. Table 3 lists the relevant values computed by the different participants.

Table 3 Case 1: Optional Case Delta Ray Conditions

Participant Index	Delta Ray Conditions	f_{ac} (Hz)	Computed R_{tot} (meters)
P1	M=1.5204, $\frac{dM}{dt}$ = 0.017991	7.42	26,531
P6	M=1.5207, $\frac{dM}{dt}$ = 0.017996	9.76	186,196
P7	M=1.5206, $\frac{dM}{dt}$ = 0.017996	7.63	27,335

Figure 16 shows the focus waveforms computed by the three participants. Figure 16(a) depicts the comparison of the incoming waveform as predicted by the three participants. This shows small differences in the incoming waveform owing to the slight differences in the computed delta ray conditions. Figure 16(b) depicts the evanescent wave comparison at $\overline{Z} = -1$, which corresponds to a distance of one diffraction boundary layer thickness below the caustic surface. Figures 16(c) and 16(d) show the comparison of the focus and post-focus signatures at non-dimensional distances of $\overline{Z} = 0$ and

$\overline{Z} = 1$ respectively. These figures show that the focal signatures (at $\overline{Z} = 1$) are similar in character but differing slightly in the shock pressure rise magnitude and the duration of the signature. Figure 16(d) shows the post-focal signatures at $\overline{Z} = 1$, where each of the participants predicted similar pressure magnitudes but they differed in terms of separation of the incoming and reflected waveforms. Table 4 lists the perceived level of loudness computed by each of the three participants at the three different locations within the LNTE computational domain. Although the loudness values are relatively close to each other on the illuminated side of the caustic surface, the loudness metrics on the evanescent side are much lower in magnitude and the differences between participants is much larger.

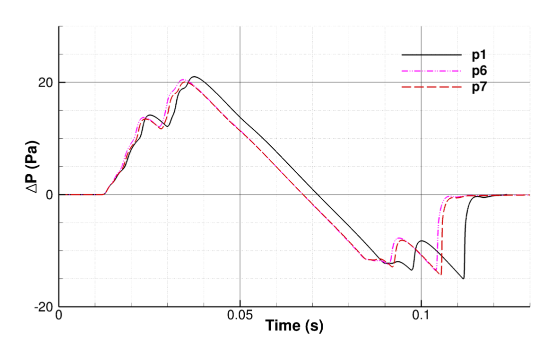

(a) **Waveforms at the interface between Burgers and LNTE.**

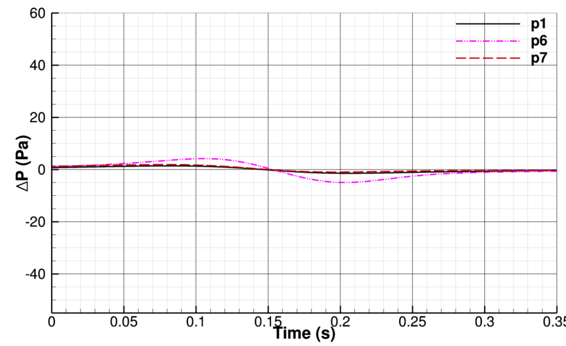

(b) **Evanescent waveforms at $\overline{Z} = -1$.**

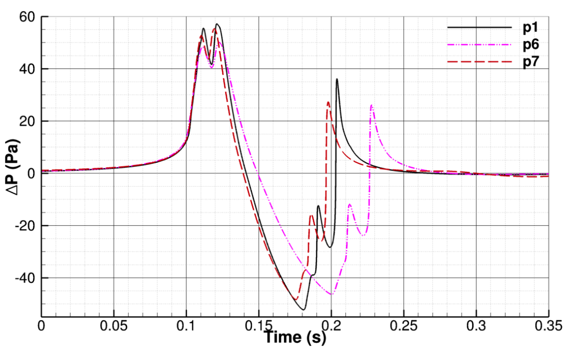

(c) **Focus Signatures at $\overline{Z} = 0$.**

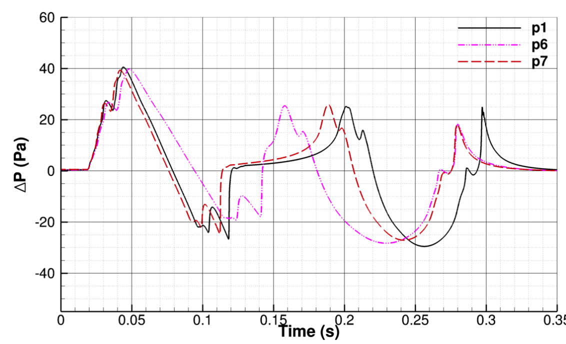

(d) **Post-focus Signatures at $\overline{Z} = 1$.**

Fig. 16 Case 1: Comparison of optional focus signatures.

In order to determine the source of the differences, a couple of additional runs were requested from the participants. In the first exercise, participant p7 was requested to use participant p1's incoming waveform to predict the signatures within the LNTE computational domain. Figure 17(a) depicts the predicted signatures at $\overline{Z} = 0$ when participant p7 predicted their own incoming waveform using their delta ray conditions, and Fig. 17(b) shows the signatures when participant p7 used participant p1's predicted incoming waveform for the LNTE solver. This behavior is observed at all locations with the LNTE computational domain, not just $\overline{Z} = 0$. Based on these results, the LNTE solution process and results are more or less identical between participant p1 and p7; the primary source of difference is the incoming waveform on the delta ray or the input to the LNTE solver.

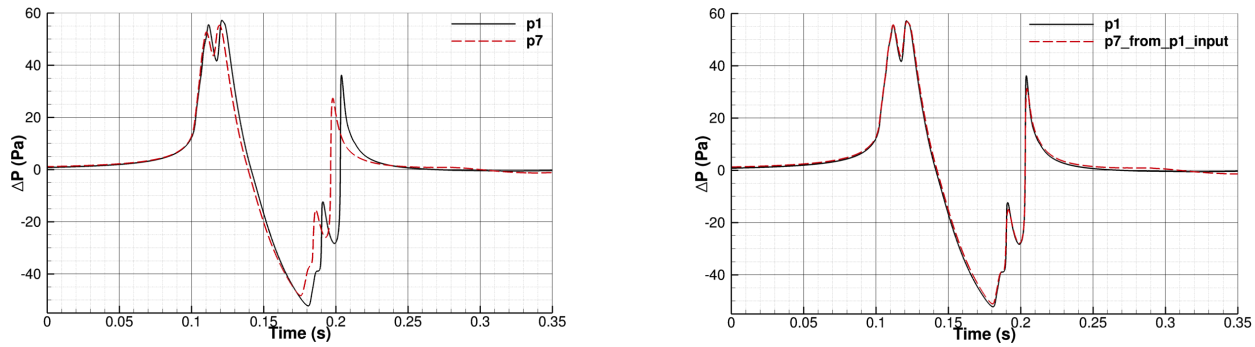

(a) **Comparison of Signatures at $\overline{Z} = 0$ for participants p1 and p7.**

(b) **Revised Comparison of Signatures at $\overline{Z} = 0$ for participants p1 and p7.**

Fig. 17 Optional Case 1: Source of the difference between participant p1 and p7.

Figure 16(d) showed that participant p6 had a shortened separation between the actual waveform and the waveform reflected off the caustic surface. Based on the interactions with participant p6, it was determined that they were using a relative radius of curvature that was inconsistent with the prescribed value of the diffraction boundary layer thickness. Using their computed $R_{tot} = 56,769$ meters and the incoming waveform characteristic frequency $f_{ac} = 12.816$ Hz, their diffraction boundary layer thickness can be computed to be 270.72 meters. To consistently compare all the waveforms at the same physical location, a $\overline{Z} = 1$ value for participants p1 and p7 is equivalent to a value of $\overline{Z} = \frac{302.4}{270.72} = 1.117$ for participant p6. Figure 18(b) plots the revised results when signatures are extracted at the same physical location rather than at the same non-dimensional value. Compared to Fig.18(a), the spread and duration comparison between participants is better. As has been mentioned earlier, the other differences are stemming from the differences in the computation of the incoming waveform on the delta ray and these differences need to be investigated in future workshops.

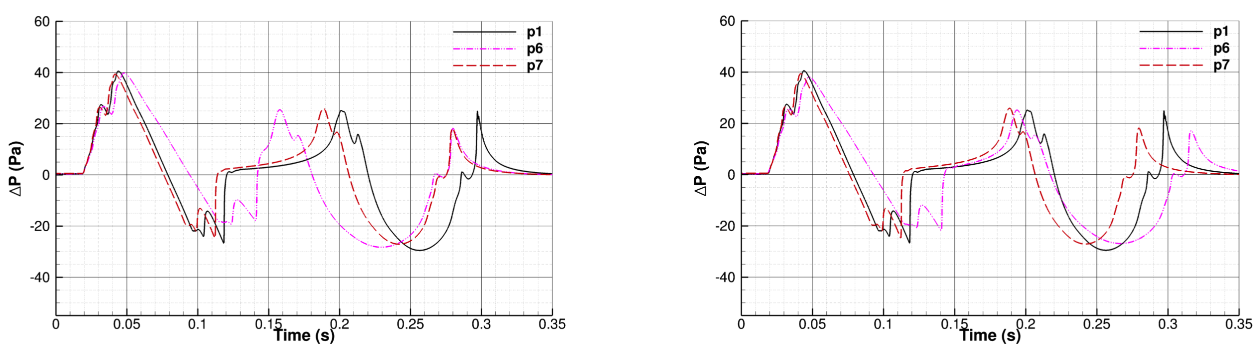

(a) **Original post-focus signatures at $\overline{Z} = 1$.**

(b) **Revised post-focus signatures at $\overline{Z} = 1$.**

Fig. 18 Case 1: Revised comparison of post-focus signatures.

Table 4 Case 1: Optional Case Loudness Values

Participant Index	$\overline{Z}$	Loudness Metrics (PLdB)
P1	-1.0, 0.0, 1.0	2.8, 101.12, 95.95
P6	-1.0, 0.0, 1.0	73.82, 96.94, 87.10
P7	-1.0, 0.0, 1.0	58.06, 96.66, 88.84

VI. Results and Discussion for Case 2: C609 Sonic Boom Comparison and Analysis

A. Ground Signatures and Loudness Metrics

Just like the previous case, Fig. 19 depicts the ground signatures corresponding to all participant submissions at some selected azimuthal angles. Overlaid on top is the mean and one standard deviation bounds from the mean waveform. Based on this plot, certain submissions that are significantly outside these bounds are termed as outliers; however, the same qualifier used earlier in Case 1 applies to these outlier cases. Figure 20 depicts the ground signatures after removing the outliers (p3, p11, and p12). Generally, if a participant submission was determined as an outlier at one azimuthal angle, it remained an outlier at all the azimuthal angles analyzed. However, there were some submissions that were outliers at a particular azimuthal angle without being an outlier at the other ray angle inclinations, such as participant p4 in Fig. 19(c). Even though the ground signatures are more tightly spaced, there are significant differences in the initial shock rise times ($\approx 40\%$) and duration ($\approx 7\%$). These kind of differences usually tend to result in quite large differences in the loudness metrics, which are discussed next.

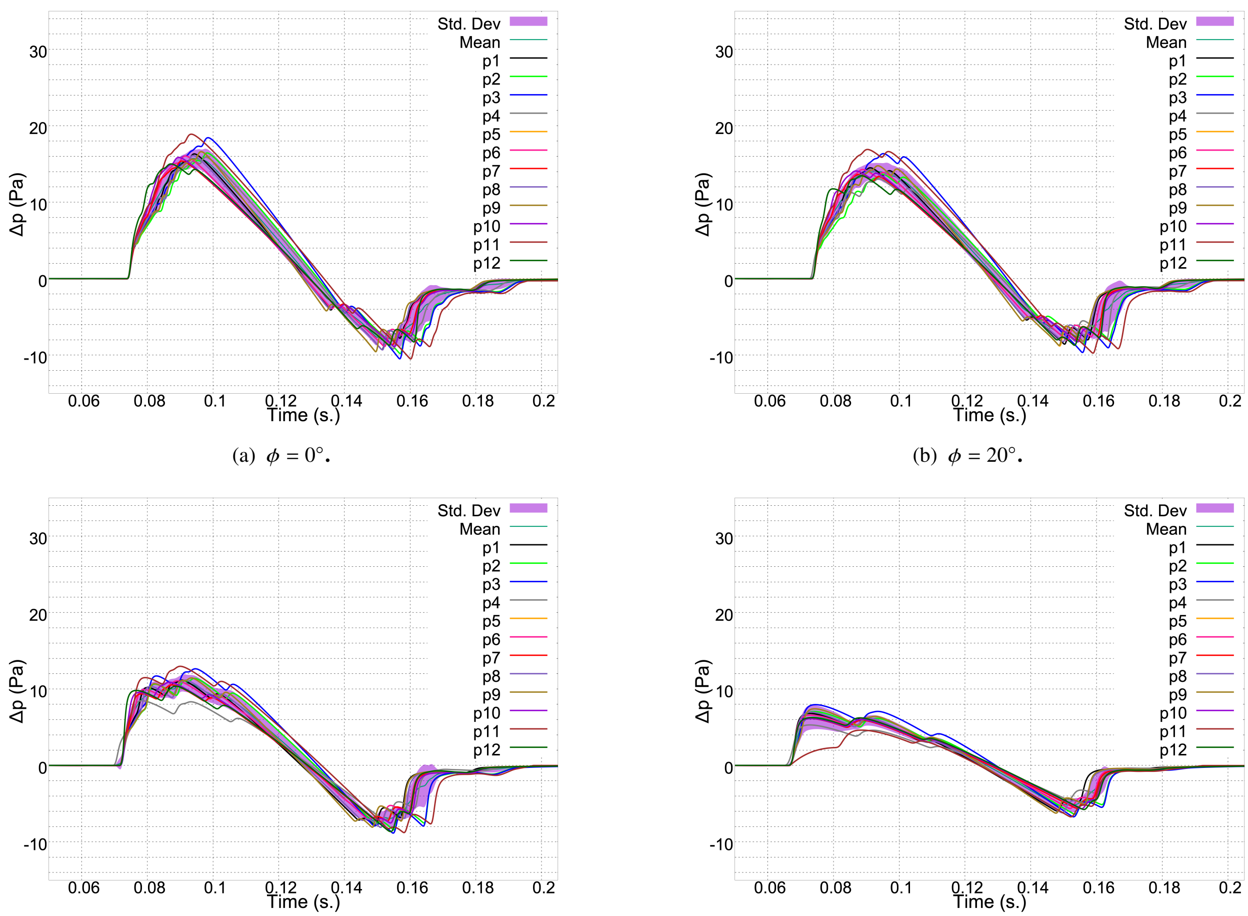

(a) $\phi = 0°$.

(b) $\phi = 20°$.

(c) $\phi = 40°$.

(d) $\phi = 60°$.

Fig. 19 Case 2: Ground signatures overlaid on 1 standard deviation from mean.

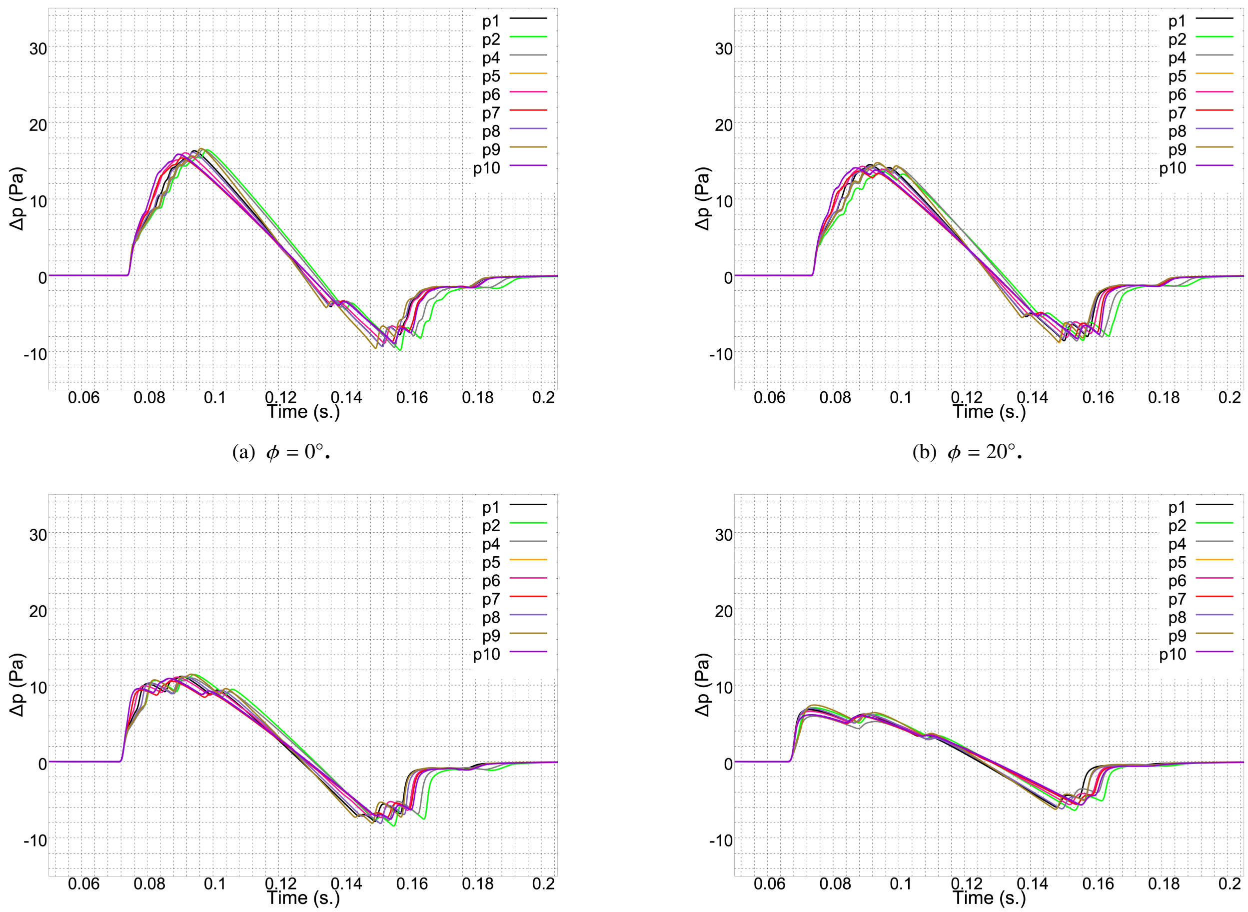

(a) $\phi = 0°$.

(b) $\phi = 20°$.

(c) $\phi = 40°$.

(d) $\phi = 60°$.

Fig. 20 Case 2: Ground signatures within 1 standard deviation.

All the loudness metrics requested are plotted together as a function of the lateral distance in Fig. 21. All the previous observations from Case 1 still hold true. However, the lateral carpet widths predicted are larger than the first case, in line with the selection of the atmospheres (see Fig. 4(b)). All the loudness metrics from all participants are clustered closer to the flight track and spread apart as the lateral distance increases on either side of the flight track. PL and ASEL have a larger spread compared to BSEL and CSEL metrics.

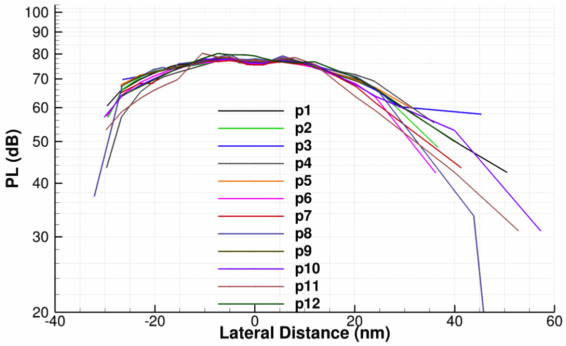

(a) **PL carpet.**

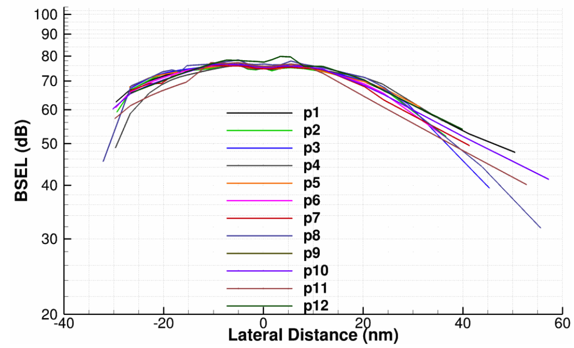

(b) **BSEL carpet.**

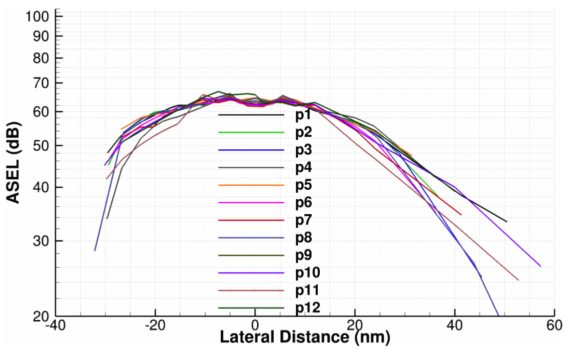

(c) **ASEL carpet.**

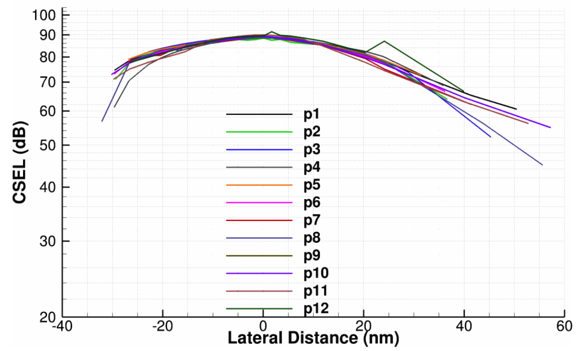

(d) **CSEL carpet.**

Fig. 21 Case 2: Loudness carpet.

In order to delineate the loudness metrics further, PL and BSEL metrics for all the participants are compared for the inner carpet, including the depiction of the discrete points that make up these plots, as seen in Figs. 22(a) and 22(b). As in the previous case, the discrete points are almost vertically aligned showing that ray paths are nearly identical for all the participants. The PL and BSEL spreads are in the range [2.5, 4.0] and [2.5, 5.5] decibels, respectively. However, once we remove the outliers identified in Fig. 19, the spread drops to [1.5, 3.0] decibels for both these metrics (see Figs. 22(c) and 22(d)). As a verification step, loudness metrics were computed from the participants' ground signatures and compared rather than using the loudness values submitted by participants. Although there was no difference in PL computed versus submitted (compare Figs. 22(c) and 22(e)), there was a noticeable difference in participant p8's submission of BSEL. With this step, Fig. 22(f) shows that the spread in BSEL further decreased to [1.0, 2.5] decibels across the inner carpet.

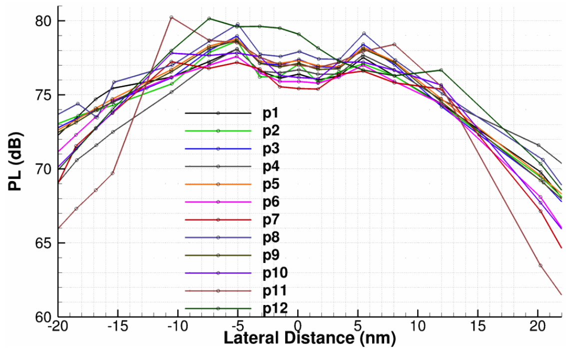

(a) **PL inner carpet.**

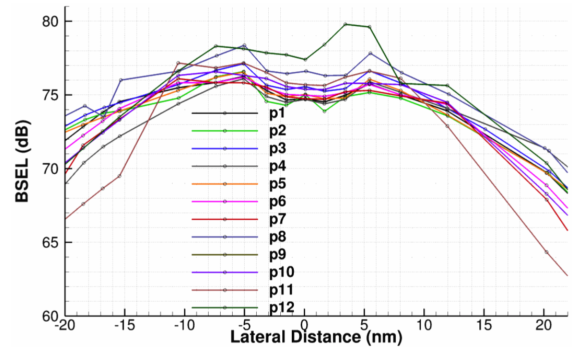

(b) **BSEL inner carpet.**

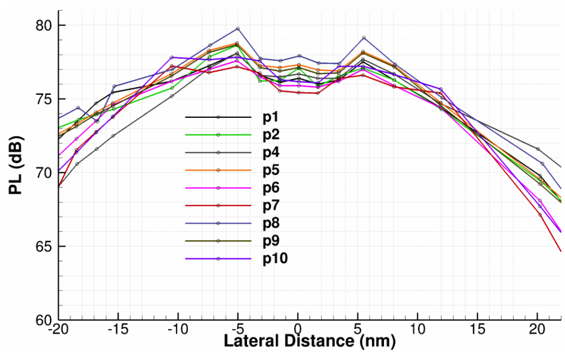

(c) **PL inner carpet with outliers removed.**

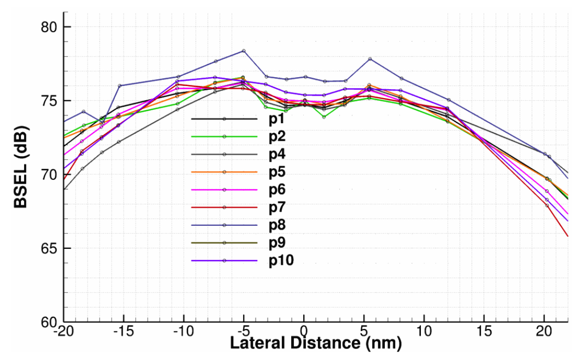

(d) **BSEL inner carpet with outliers removed.**

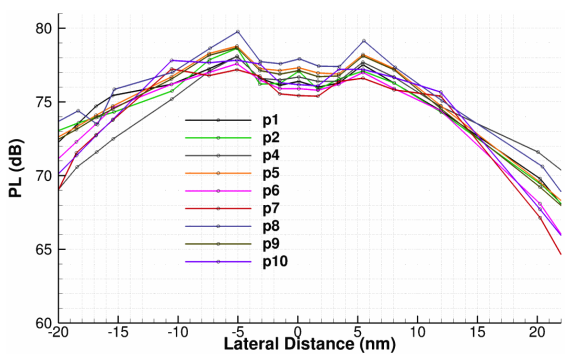

(e) **PL inner carpet: Computed Loudness.**

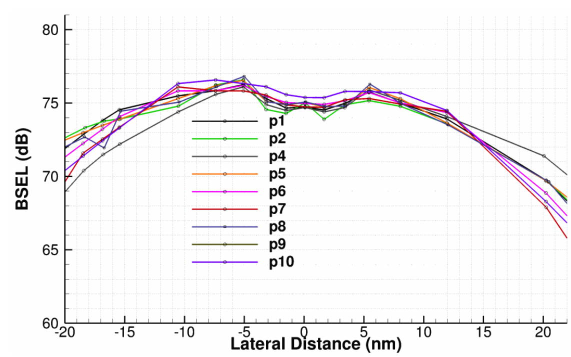

(f) **BSEL inner carpet: Computed loudness.**

Fig. 22 Case 2: Loudness inner carpet.

Propagation under standard atmosphere was requested as an optional case for C609. Figures 23(a) and 23(b) depict that under standard atmospheric conditions, participants who submitted data for these optional conditions show a spread of approximately [0, 1.0] decibels for both PL and BSEL metrics. The values are tightly spaced for BSEL compared to PL. These plots show that most of the differences being observed for the required cases are due to differences in the numerical implementation of the wind effects as well as differences in the underlying interpolation schemes that are magnified with complex waveforms that generate extremely low loudness levels.

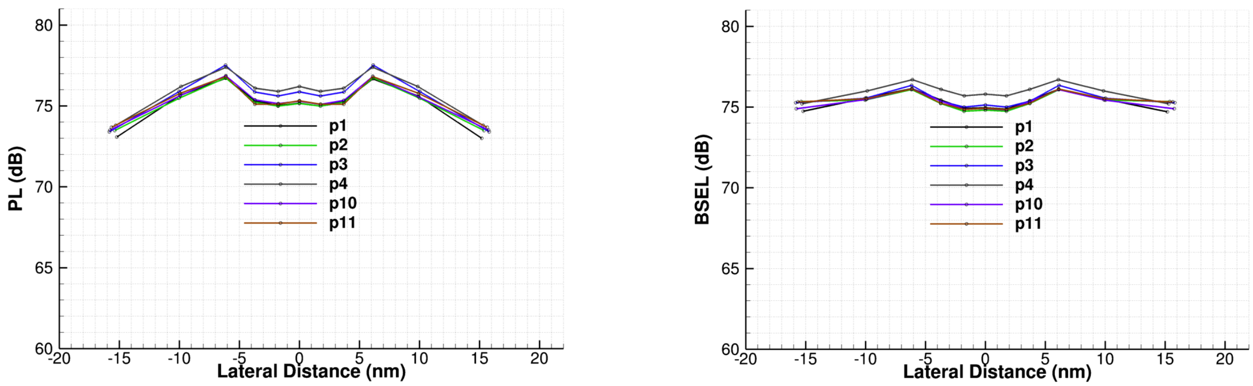

(a) **PL carpet, standard atmosphere.**

(b) **BSEL carpet, standard atmosphere.**

Fig. 23 Case 2: Loudness carpet with standard atmosphere.

B. Statistical Analysis

The Case 2 box plot results in Fig. 24 show a higher amount of spread and variation in the data compared to Case 1, especially farther off-track. The atmosphere was chosen to result in a physically wide carpet, and rays from azimuthal angles of -62° to +70° are predicted to reach the ground for all participants. Seven out of twelve participants also predicted sonic booms emanating from -64°, although the results are not shown because the levels are so low (PL median of 47.3 dB and BSEL median of 51.3 dB). The carpet is asymmetric, although the maximum values are still found at ± 30°. In this case, the spread in the BSEL results is similar to that for PL, except for tighter groupings toward the lateral edges of the carpet.

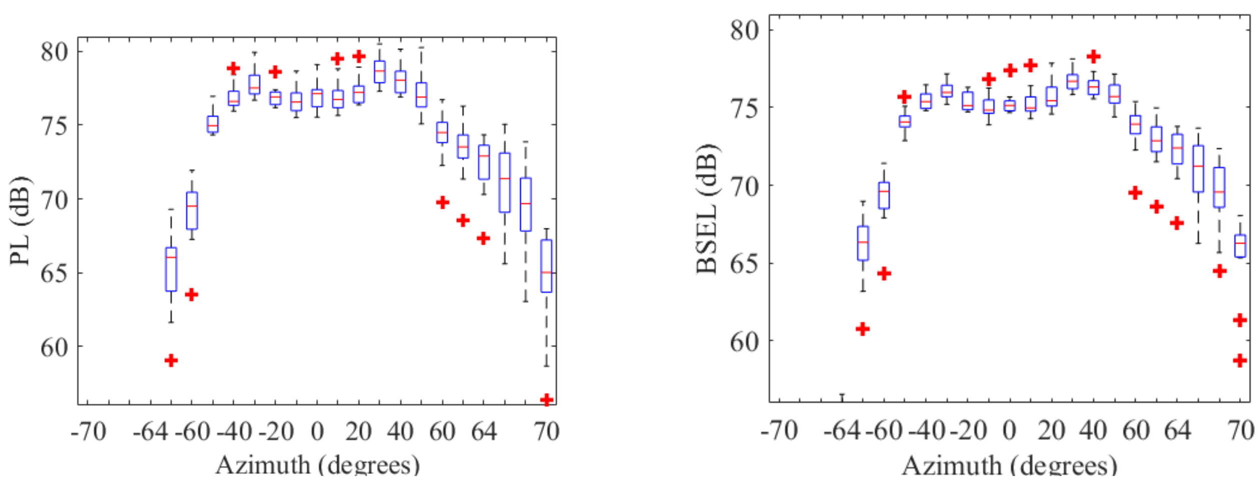

(a) **PL.**

(b) **BSEL.**

Fig. 24 Case 2 PL and BSEL boxplots across the carpet.

The standard deviation of Case 2 predicted values across participants for each azimuthal angle is shown in Fig. 25 for each of the six metrics considered. As in Case 1, all metrics were re-calculated from the submitted waveforms using the same loudness code. The standard deviations with PL and ASEL are generally the largest, ranging from 0.7 dB to 7 dB. The largest values occur toward the lateral edges of the carpet, with higher standard deviations at the negative azimuthal side, where only a fraction of participants computed waveforms for -64°. The other metrics exhibit similar trends, but at lower levels, with DSEL having the lowest standard deviation values.

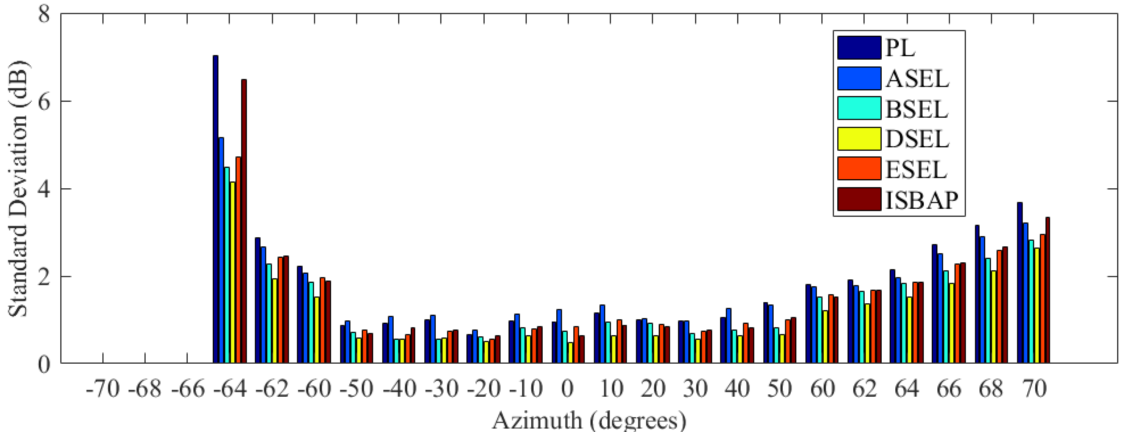

Fig. 25 Case 2 standard deviation of metric values across the carpet.

C. Spectral Analysis

Spectral plots of the waveforms for the undertrack case of $\phi = 0°$ are included in Fig. 26(a). Although most results are very similar, the p8 spectrum has higher SPL values above 1 kHz. The loudness spectra in Fig. 26(b) show a small increase in loudness for p8 above 1 kHz, which contributes to a slightly higher PL value, although it is not considered an outlier.

For the phi angle of +70°, the spectra and loudness spectra in Fig. 27 show less agreement between participants. The loudness spectra for p4 and p11 appear to be lower than the others, and the resulting PL for p4 is the outlier shown in Fig. 24(a) at 70°. The higher energy at high frequencies for p8 is less significant at this angle than undertrack.

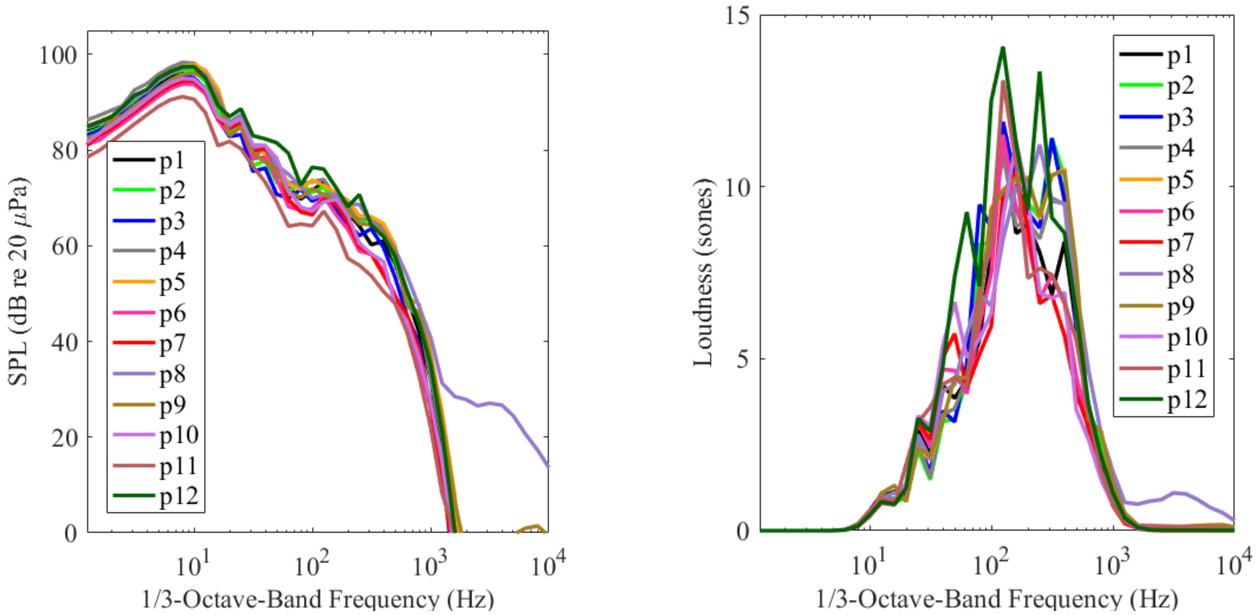

(a) **SPL.** (b) **Loudness.**

Fig. 26 Case 2 Sound Pressure Level (SPL) spectra and loudness spectra for ϕ = 0°.

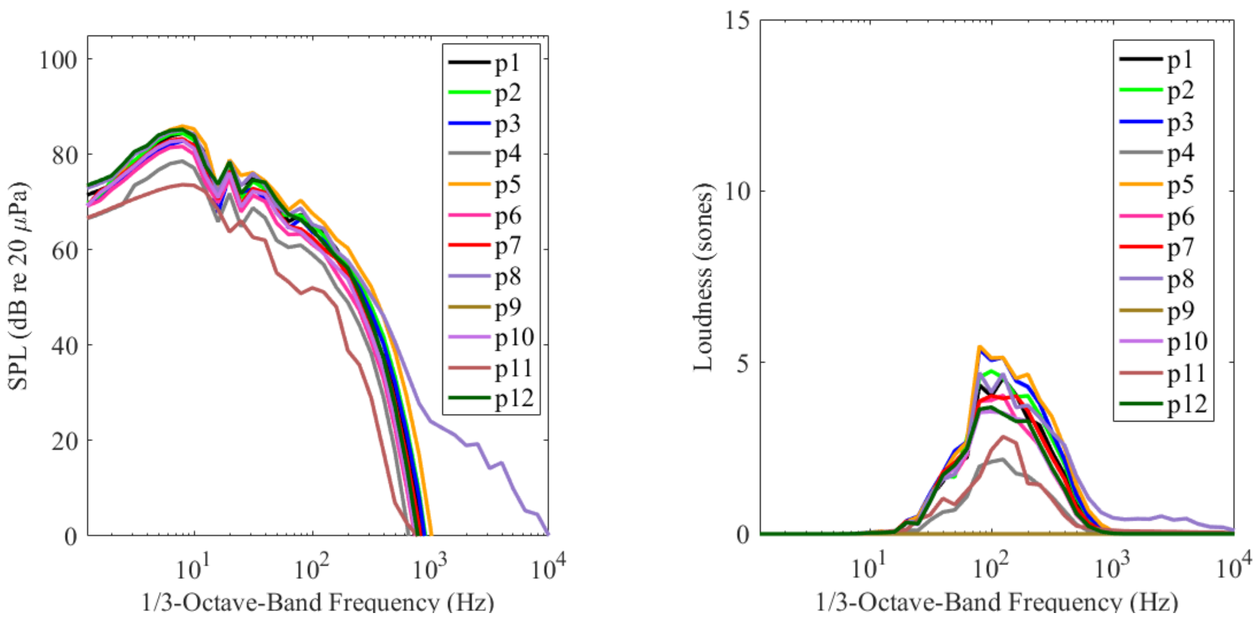

(a) **SPL.** (b) **Loudness.**

Fig. 27 Case 2 Sound Pressure Level (SPL) spectra and loudness spectra for ϕ = 70°.

VII. Lessons Learned and Recommendations

Figure 28 shows the loudness carpet in terms of the PL metric for each of the cases corresponding to SBPW2 and SBPW3. Also shown are the bands of one standard deviation from the mean for each of the ensembles. The following observations can be made from this plot:

1) The loudness levels of SBPW3 are much lower compared to SBPW2. Given that loudness values are on a logarithmic scale, this reduction roughly translates to SBPW3 cases having the equivalent of about $\frac{1}{32}$ and $\frac{1}{4}$ of the over-pressures of SBPW2 LM1021 and SBPW2 Axibody configurations, respectively.
2) SBPW3 submissions requested data across the entire carpet, whereas SBPW2 only requested data at 3 azimuthal angles for each case.
3) The standard deviation significantly reduced compared to the SBPW2 LM1021 configuration.

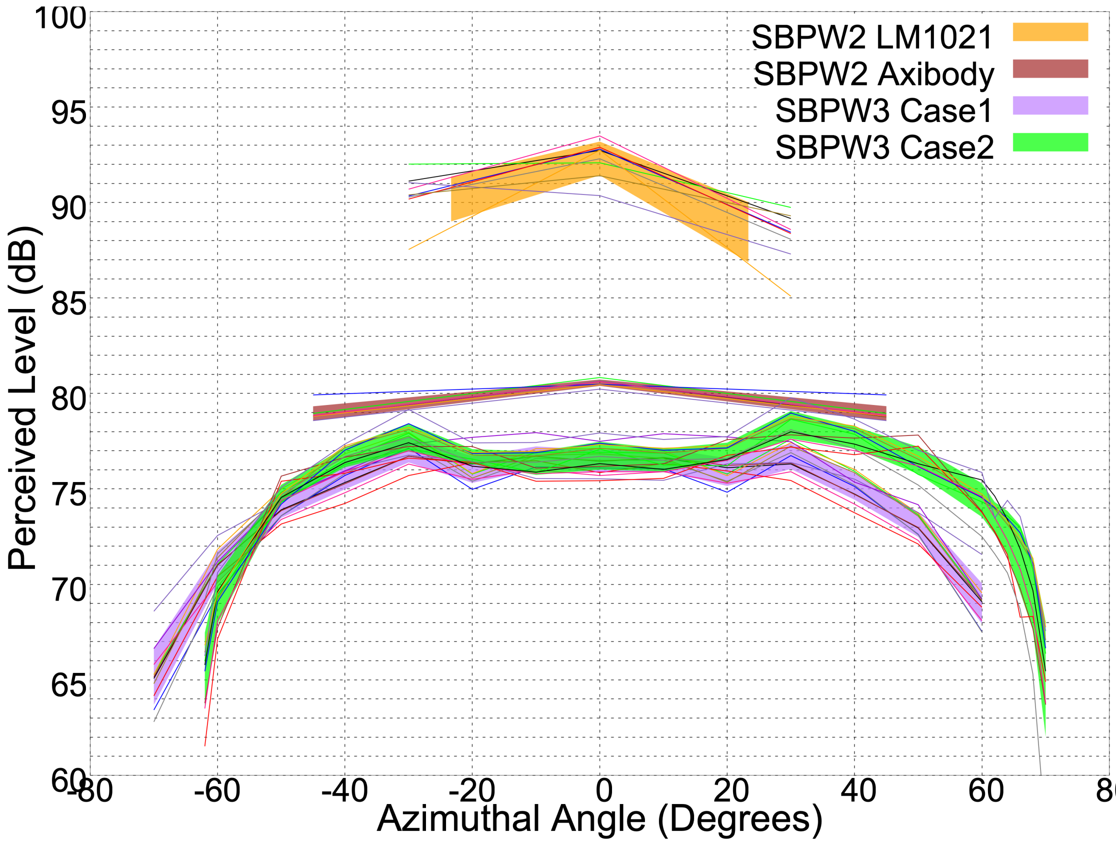

Fig. 28 Comparison between SBPW2 and SBPW3 propagation cases.

These trends show that the sonic boom propagation community has made steady progress in refining their prediction capabilities even in the face of increasingly complex and extremely low loudness levels.

The signature duration differences observed between participants (see Figs. 7 and 19(a)) forced us to investigate the source of these differences. As part of that effort, a few participants were requested to submit their dimensional, pressure (Pa) vs. time (seconds), near-field waveforms for Case 1. The idea was to make sure participants were using similar approaches in accounting for the azimuthal and wind effects in determining the starting waveform for atmospheric propagation along the ray tubes. Figures 29(a) and 29(b) depict these dimensional waveforms from selected participants at azimuthal angles of 0° and 60°, respectively. It is clear that participants differ at the initial location for windy cases owing to differences in determining them relative to the airmass or relative to the fixed ground. Once this discrepancy is resolved, the differences between participants would be further reduced. Future workshops should either provide a consistent approach to compute these initial dimensional waveforms or the dimensional waveforms should be provided.

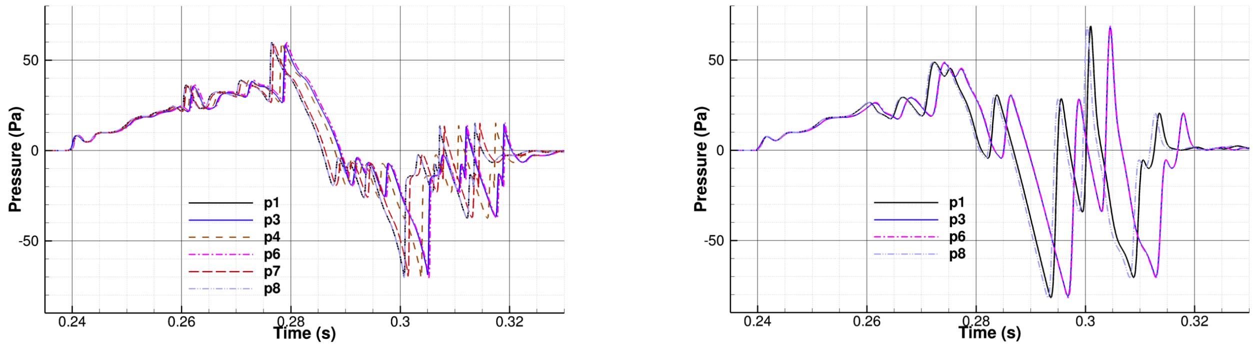

(a) **Pressure-time near-field at** 0°.

(b) **Pressure-time near-field at** 60°.

Fig. 29 Case 1: Comparison of pressure versus time in the near-field.

VIII. Concluding Remarks

The Third AIAA Sonic Boom Prediction Workshop was a huge success in terms of evaluating and comparing results from multiple sonic boom propagation models for multiple aircraft concepts under measured and standard atmospheric conditions. The differences between results are documented and the associated statistics are presented. Since participants were free to use their best practices and methods, the authors took a deeper look at potential sources of the differences between submissions. Based on this analysis, it was determined that the differences in loudness metrics may be significantly reduced if the underlying conventions are explicitly stated and adhered to by all the participants.

This workshop and analysis provides information to industry, research organizations, and regulators about sonic boom predictions under realistic atmospheric conditions and highlights the areas where further work may be necessary to bring results into better agreement. The workshops attract participation from a variety of sonic boom professionals that are engaged in discussing the current state-of-the-art numerical sonic boom prediction models, identifying the current modeling gaps, formulating new and increasingly more complex test cases, and documenting the results for future efforts and generations. Continuation of this effort is proposed to inform the development of a noise certification standard for civil supersonic aircraft.

Acknowledgments

This work was supported by the NASA Advanced Air Vehicles Program, Commercial Supersonic Technology (CST) Project. The authors would like to thank the AIAA boom prediction committee for organizing the workshops. Many thanks are also due to the workshop participants for investing their valuable time in running the cases, being willing to provide additional data as requested, and agreeing to have their data published anonymously. The authors also wish to acknowledge Will Doebler's efforts in down-selecting the atmospheric profiles used in the propagation cases.

References

[1] Park, M. A., and Morgenstern, J. M., "Summary and Statistical Analysis of the First AIAA Sonic Boom Prediction Workshop," *AIAA Journal of Aircraft*, Vol. 53, No. 2, 2016, pp. 578–598. doi:10.2514/1.C033449.

[2] Park, M. A., and Nemec, M., "Near Field Summary and Statistical Analysis of the Second AIAA Sonic Boom Prediction Workshop," *AIAA Journal of Aircraft*, Vol. 56, No. 3, 2019, pp. 851–875. doi:10.2514/1.C034866.

[3] Rallabhandi, S. K., and Loubeau, A., "Summary of Propagation Cases of the Second AIAA Sonic Boom Prediction Workshop," *AIAA Journal of Aircraft*, Vol. 56, No. 3, 2019, pp. 876–895. doi:10.2514/1.C034805.

[4] Park, M. A., and Carter, M. B., "Nearfield Summary and Analysis of the Third AIAA Sonic Boom Prediction Workshop C608 Low Boom Demonstrator," AIAA SciTech 2021 American Institute of Aeronautics and Astronautics, Reston, VA (submitted for publication).

[5] Carter, M. B., and Park, M. A., "Near Field Summary and Analysis of the Third AIAA Sonic Boom Workshop Shock-Plume Interaction Case," AIAA SciTech 2021 American Institute of Aeronautics and Astronautics, Reston, VA (submitted for publication).

[6] George, A. R., "Reduction of Sonic Boom by Azimuthal Redistribution of Overpressure," AIAA Paper 68–159, 1968.

[7] Page, J. A., and Plotkin, K. J., "An Efficient Method for Incorporating Computational Fluid Dynamics into Sonic Boom Prediction," AIAA Paper 91–3275, 1991.

[8] Rallabhandi, S. K., and Mavris, D. N., "New Computational Procedure for Incorporating Computational Fluid Dynamics into Sonic Boom Prediction," *AIAA Journal of Aircraft*, Vol. 44, No. 6, 2007, pp. 1964–1971.

[9] Saito, Y., Ukai, T., Miyakoshi, K., Ohtani, K., and Obayashi, S., "Sonic Boom Estimation using the Multipole Method for Free-Flight Experiments," AIAA Paper 2014–368, 2014.

[10] Cowart, R., "Status of Certification Procedures for Quiet Supersonic Flight," AIAA Aviation 2019, Invited Oral Presentation, Special Session: Commercial Supersonic Technologies I American Institute of Aeronautics and Astronautics, 2019.

[11] Saha, S., Moorthi, S., Pan, H.-L., et al., "The NCEP Climate Forecast System Reanalysis," *American Meteorological Society*, 2010, pp. 1015–1057. doi:10.1175/2010BAMS3001.1.

[12] Stevens, S., "Perceived Level of Noise by Mark VII and Decibels(E)," *Journal of the Acoustical Society of America*, Vol. 51, No. 2, 1972, pp. 575–601.

[13] Leatherwood, J. D., Sullivan, B. M., Shepherd, K. P., McCurdy, D. A., and Brown, S. A., "Summary of Recent NASA Studies of Human Response to Sonic Booms," *The Journal of the Acoustical Society of America*, Vol. 111, No. 1, 2002, pp. 586–598. doi:10.1121/1.1371767.

[14] Loubeau, A., Naka, Y., Cook, B. G., Sparrow, V. W., and Morgenstern, J. M., "A New Evaluation of Noise Metrics for Sonic Booms Using Existing Data," *2nd International Sonic Boom Forum*, 20th International Symposium on Nonlinear Acoustics, 2015.

[15] Joseph A. Salamone, I., Sparrow, V. W., and Plotkin, K. J., "Solution of the Lossy Nonlinear Tricomi Equation Applied to Sonic Boom Focusing," *AIAA Journal*, Vol. 51, No. 7, 2013. doi:10.2514/1.J052171.

[16] Page, J. A., Plotkin, K., Hobbs, C., Sparrow, V., Salamone, J., Cowart, R., Elmer, K., Welge, H. R., Ladd, J., Maglieri, D., and Piacsek, A., "Superboom Caustic Analysis and Measurement Program (SCAMP) Final Report," NASA CR-2015-218871, Langley Research Center, Aug. 2015. doi:2060/20150019419.

[17] Kanamori, M., Takahashi, T., and Makino, Y., "Effect of Low-Boom Waveform on Focus Boom Using Lossy Nonlinear Tricomi Equation Analysis," *AIAA Journal*, Vol. 55, No. 6, 2017. doi:10.2514/1.J055226.